

Model-Based Adaptive Control of Modular Multilevel Converters

Davide Tebaldi*, Roberto Zanasi

^a*University of Modena and Reggio Emilia, Via Pietro Vivarelli 10 - int.
1, Modena, 41125, Italy*

Abstract

Electrical power conversions are common in a large variety of engineering applications. With reference to AC/DC and DC/AC power conversions, a strong research interest resides in multilevel converters, thanks to the many advantages they provide over standard two-level converters. In this paper, we first provide a power-oriented model of Modular Multilevel Converters (MMCs), followed by a detailed harmonic analysis. The model is given in the form of a block scheme that can be directly implemented in the Matlab/Simulink environment. The performed harmonic analysis gives a deep and exact understanding of the different terms affecting the evolution of the voltage trajectories in the upper and lower arms of the converter. Next, we propose a new model-based adaptive control scheme for MMCs. The proposed control allows to determine the optimal average capacitor voltages reference in real-time, thus allowing to properly track the desired load current while minimizing the harmonic content in the generated load current itself.

Keywords: Model-Based Adaptive Control, Harmonic Analysis, Modeling, Modular-Multilevel Converters, Power Electronics, Simulation.

1. Introduction

Power conversions are performed in many engineering applications, including power grids [1]-[2], hybrid electric vehicles [3]-[4] and many other

*Corresponding author

Email addresses: davide.tebaldi@unimore.it (Davide Tebaldi),
roberto.zanasi@unimore.it (Roberto Zanasi)

applications involving electric motor drives. The devices which are responsible for performing such power conversions are power converters, and can be mainly classified into DC/DC [5]-[7], AC/DC and DC/AC [8]-[10] power converters. Multilevel converter topologies offer many pros when compared to two-level power converters [11], including distortion reduction in the output voltage waveform and in the absorbed input current as well as a reduced dv/dt effect. Different multilevel converter topologies are available in the literature, including cascaded H-bridges multilevel converters [12]-[13], converter topologies with flying capacitors [10], [14]-[15], and Modular Multilevel Converters (MMCs) [16]-[24]. In this paper, MMCs in half-bridge configuration are subject of study.

The first operation to be performed is a correct and accurate modeling of the considered multilevel converter topology, for which many different approaches can be found in the literature. Modular Multilevel Matrix Converters are modeled in [16] in a matrix form with the definition of a power-capacitor voltage model and of a voltage-current model. A state-space model of Modular Multilevel Converters is proposed in [17] instead. In the present paper, Modular Multilevel Converters are modeled using a new and effective approach which is based on the Power-Oriented Graphs (POG) modeling technique [25]. In the literature, two additional main graphical techniques for modeling physical systems can be found: Bond Graphs (BG) [26]-[27] and Energetic Macroscopic Representation (EMR) [18], [28]. In the present paper, the POG technique is employed as a tool to develop the proposed converter model, since it provides user-friendly block schemes which are directly implementable in the Simulink environment using simple blocks available from standard libraries, such as integrators and gains for instance. Some examples where the POG technique can be effectively applied can be found in [10] for the modeling of multilevel flying-capacitor converters, in [29] for the modeling of Permanent Magnet Synchronous Motors, in [3] for the modeling of planetary gear sets and in [30] for the modeling of multiphase diode bridge rectifiers. In this paper, two MMC models are derived: a complete model and an average model. The complete model is very suitable for a detailed simulation of the converter dynamics and provides the full differential equations describing it, whereas the average model proves to be very suitable for deriving the proposed new model-based adaptive control of MMCs, thanks to the detailed harmonic analysis performed on it.

The next important step consists in properly controlling the considered multilevel topology. The control of MMC can be divided into two different

parts [19]: the control of the power and current inside the MMC and the voltage balancing control. However, addressing all these control objectives is not an easy task. The full-order nonlinear control of the MMC is addressed in [19] without considering the voltage balancing issue. In [20], a novel modulation scheme and a closed-loop method for voltage balancing are proposed. In [21], the authors propose a new modulation technique named Integral Modulation Technique to achieve load current control and voltage balancing, whereas a control approach based on Weighted Model Predictive Control (WMPC) for a half-bridge MMC is proposed in [22]. However, this latter approach only relies on MPC to minimize an objective function to achieve both voltage balancing and load current control and does not fully analyze the complex dynamics of MMC. A control approach based on MPC is also proposed in [23], named Model Predictive Direct Current Control, proposing a cost function that also accounts for the number of switching transitions. An interesting dynamic analysis of the modular multilevel converter is proposed in [24] where, assuming that the output current tracks the desired profile, the nonlinear model of the MMC is derived. The system equilibrium points are then computed neglecting the oscillatory terms, based on which the control of the circulating current is evinced. In the present paper, we introduce the following new contributions which, to the best of our knowledge, have not yet been fully addressed in the literature: 1) the proposal of a compact block scheme modeling MMCs. The block scheme is directly implementable in the Matlab/Simulink environment using simple blocks which are available in standard Simulink libraries, such as integrators and gains. The proposed model is also verified against the PLECS (Piecewise Linear Electrical Circuit Simulation) simulator [31]. 2) the development of an harmonic analysis in which all the oscillatory terms are taken into account. This enables a deep and exact understanding of the MMC dynamics, based on which we can determine the optimal tracking reference for the circulating current in order to make the average capacitor voltages follow the desired reference. 3) the exact computation of the optimal voltage reference for the average capacitor voltages in the upper and lower arms of the converter. Such optimal voltage reference is the minimum value which is strictly necessary to properly track the desired load current while, at the same time, minimizing the harmonic content in the generated load current itself. 4) the proposal of a new model-based adaptive control which allows to effectively achieve all the control objectives at the same time: a) balancing of the capacitor voltages; b) tracking of the optimal voltage reference for the average capacitor voltages

in order to minimize the harmonic content in the load current; c) tracking of the desired load current profile.

One of the new important concepts that we introduce in this paper is that of adaptively varying the average capacitor voltages in the upper and lower arms of the MMC, which is what makes the proposed model-based control adaptive to the operating conditions. The average capacitor voltages are properly controlled to follow an optimal voltage reference using the circulating current, where such optimal voltage reference is adapted in real-time as a function of the desired load current. This represents a crucial advantage with respect to maintaining the average capacitor voltages at a constant value, as it is typically done in literature, because it allows to reduce the harmonic content in the generated load current whenever the operating conditions allow it. This is done by minimizing the level-to-level distance in the commutating voltage signals, thus enhancing all the intrinsic main advantages of multilevel converters.

The remainder of this paper is structured as follows. The complete dynamic model of MMCs is derived in Sec. 2.1 and verified in Sec. 2.2. An average model of the converter is proposed in Sec. 2.3, which will be fundamental for the harmonic analysis and for the model-based adaptive control derivation. The Control Problem is addressed in Sec. 3 based on the model transformation illustrated in Sec. 2.4. The capacitor voltages balancing problem in the upper and lower arms of the converter is addressed in Sec. 3.1, whereas the control of the average capacitor voltages and of the load current is described in Sec. 3.2 and in Sec. 3.3 using the proposed model-based adaptive control. Simulation results showing the effectiveness of the proposed control are reported and discussed in Sec. 4, whereas the conclusions of this work are given in Sec. 5. Finally, the detailed calculations employed when performing the system harmonic analysis are reported in App. A, App. B, App. C, App. D, App. E and App. F.

2. Dynamic Model of Modular Multilevel Converters

The circuit diagram of a MMC with n of capacitors on each arm is shown in Fig. 1. The switches reported in the figure are supposed to be in half-bridge configuration. The complete dynamic model of the MMC is derived in Sec. 2.1 and verified in Sec. 2.2 against the PLECS circuit simulator. Next, an average model of the MMC capacitive part which is suitable for the

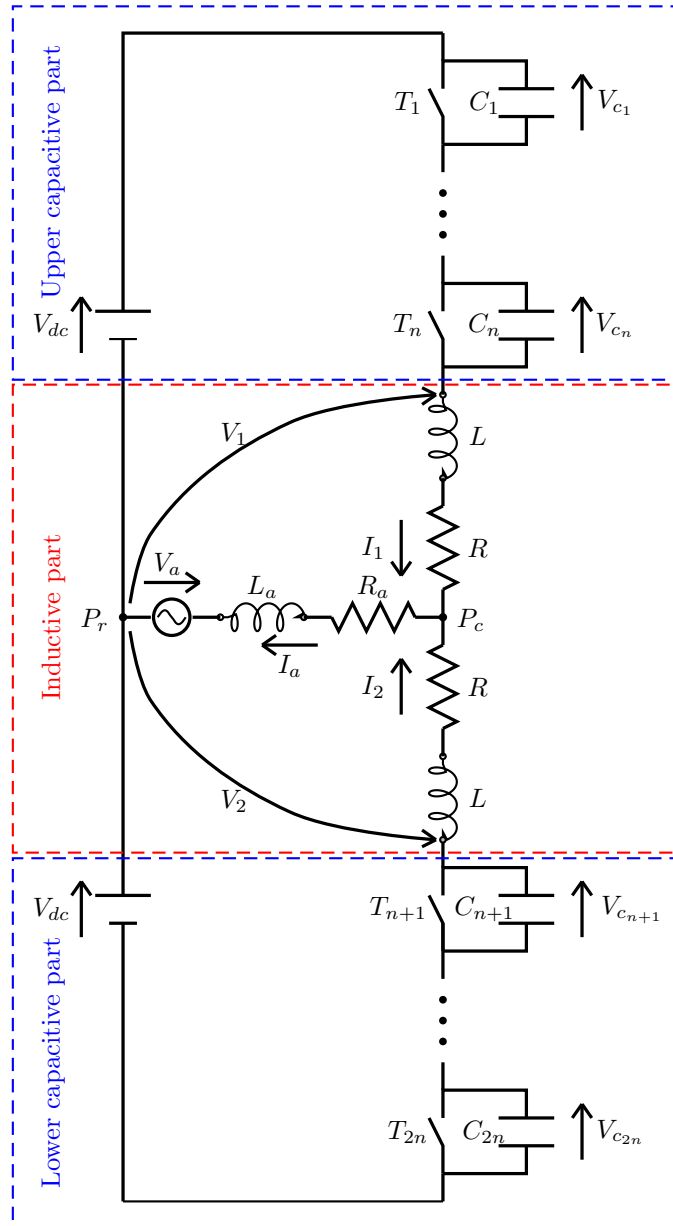


Figure 1: Circuit diagram of the considered Modular Multilevel Converter.

MMC harmonic analysis and for describing the model-based adaptive control proposed in this paper is derived in Sec. 2.3.

2.1. Full Dynamic Model of Modular Multilevel Converters

The dynamic model of the MMC inductive part can be expressed as $\mathbf{L}_L \dot{\mathbf{I}}_L = \mathbf{A}_L \mathbf{I}_L + \mathbf{V}_C + \mathbf{b}_L V_a$:

$$\underbrace{\begin{bmatrix} L + L_a & L_a \\ L_a & L + L_a \end{bmatrix}}_{\mathbf{L}_L} \dot{\mathbf{I}}_L = - \underbrace{\begin{bmatrix} R + R_a & R_a \\ R_a & R + R_a \end{bmatrix}}_{\mathbf{A}_L} \underbrace{\begin{bmatrix} I_1 \\ I_2 \end{bmatrix}}_{\mathbf{I}_L} + \underbrace{\begin{bmatrix} V_1 \\ V_2 \end{bmatrix}}_{\mathbf{V}_C} + \underbrace{\begin{bmatrix} -1 \\ -1 \end{bmatrix}}_{\mathbf{b}_L} V_a, \quad (1)$$

where R , L are the resistance and the inductance in the lower and upper arms of the converter; R_a , L_a are the load resistance and the load inductance; I_2 , I_1 are the currents flowing in the lower and upper arms of the converter; V_2 , V_1 are the commutating voltages defined as in Fig. 1, and V_a is a load sinusoidal voltage source, see Fig. 1. The dynamic model of the MMC capacitive part can be expressed as $\mathbf{L}_c \dot{\mathbf{v}}_c = \mathbf{T}_{12} \mathbf{I}_L$, $\mathbf{V}_C = -\mathbf{T}_{12}^T \mathbf{v}_c + \mathbf{d}_c V_{dc}$:

$$\underbrace{\begin{bmatrix} \mathbf{C}_1 & \mathbf{0} \\ \mathbf{0} & \mathbf{C}_2 \end{bmatrix}}_{\mathbf{L}_c} \dot{\mathbf{v}}_c = \underbrace{\begin{bmatrix} \mathbf{T}_1 & \mathbf{0} \\ \mathbf{0} & -\mathbf{T}_2 \end{bmatrix}}_{\mathbf{T}_{12}} \underbrace{\begin{bmatrix} I_1 \\ I_2 \end{bmatrix}}_{\mathbf{I}_L}, \quad (2) \quad \underbrace{\begin{bmatrix} V_1 \\ V_2 \end{bmatrix}}_{\mathbf{V}_C} = -\mathbf{T}_{12}^T \underbrace{\begin{bmatrix} \mathbf{v}_{c1} \\ \mathbf{v}_{c2} \end{bmatrix}}_{\mathbf{v}_c} + \underbrace{\begin{bmatrix} 1 \\ -1 \end{bmatrix}}_{\mathbf{d}_c} V_{dc}, \quad (3)$$

where

$$\mathbf{C}_1 = \begin{bmatrix} C_1 & \cdots & 0 \\ \vdots & \ddots & \vdots \\ 0 & \cdots & C_n \end{bmatrix}, \mathbf{C}_2 = \begin{bmatrix} C_{n+1} & \cdots & 0 \\ \vdots & \ddots & \vdots \\ 0 & \cdots & C_{2n} \end{bmatrix}, \mathbf{v}_{c1} = \begin{bmatrix} V_{c1} \\ \vdots \\ V_{cn} \end{bmatrix}, \mathbf{v}_{c2} = \begin{bmatrix} V_{c_{n+1}} \\ \vdots \\ V_{c_{2n}} \end{bmatrix}, \mathbf{T}_1 = \begin{bmatrix} T_1 \\ \vdots \\ T_n \end{bmatrix}, \mathbf{T}_2 = \begin{bmatrix} T_{n+1} \\ \vdots \\ T_{2n} \end{bmatrix}. \quad (4)$$

The signals T_i , for $i \in \{1, 2, \dots, 2n\}$, are the control variables that define the state of the switches (on/off) and the use (no/yes) of the capacitors C_i in the definition of the voltages V_1 and V_2 : a) if $T_i = 0$, the i -th switch is on and the voltage V_{c_i} of capacitor C_i is not used in the Kirchhoff's Voltage Law in (3); b) if $T_i = 1$, the i -th switch is off and the voltage V_{c_i} of capacitor C_i is used in the Kirchhoff's Voltage Law in (3). By combining together systems (1)-(3), the following $\mathbf{L} \dot{\mathbf{x}} = \mathbf{A} \mathbf{x} + \mathbf{B} \mathbf{u}$ complete dynamic model of the MMC is obtained:

$$\underbrace{\begin{bmatrix} \mathbf{L}_c & \mathbf{0} \\ \mathbf{0} & \mathbf{L}_L \end{bmatrix}}_{\mathbf{L}} \dot{\mathbf{x}} = \underbrace{\begin{bmatrix} \mathbf{0} & \mathbf{T}_{12} \\ -\mathbf{T}_{12}^T & \mathbf{A}_L \end{bmatrix}}_{\mathbf{A}} \underbrace{\begin{bmatrix} \mathbf{v}_c \\ \mathbf{I}_L \end{bmatrix}}_{\mathbf{x}} + \underbrace{\begin{bmatrix} \mathbf{0} & \mathbf{0} \\ \mathbf{d}_c & \mathbf{b}_L \end{bmatrix}}_{\mathbf{B}} \underbrace{\begin{bmatrix} V_{dc} \\ V_a \end{bmatrix}}_{\mathbf{u}}. \quad (5)$$

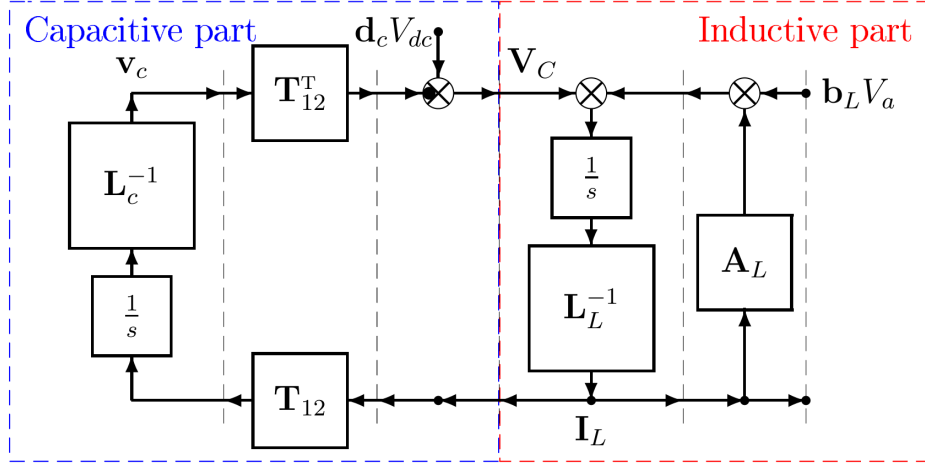


Figure 2: Block scheme of the complete MMC dynamic model.

Table 1: Parameters and initial conditions of the proposed model (5) and of the PLECS model in Fig. 3.

$L = 10$ [mH]	$R = 0.1$ [Ω]	$C_i = 1000$ [μ F]
$L_a = 50$ [mH]	$R_a = 19$ [Ω]	$V_a = 10 \sin(2\pi 50 t + \pi/6)$ [V]
$n = 3$	$V_{dc} = 250$ [V]	$T_s = 10^{-4}$ [s]
$I_{1_0} = I_{2_0} = I_{a_0} = 0$ [H],		$V_{c_{1_0}}, \dots, V_{c_{6_0}} = 110$ [V]

The order m of the dynamic system (5) is $m = 2n + 2$. A very compact block scheme of system (5) is shown in Fig. 2, having the interesting feature of being directly implemented in the Simulink environment using simple blocks which are available in standard Simulink libraries [25].

2.2. Model Verification

The MMC model proposed in (5) and in Fig. 2 has been tested against one of the most widespread platforms for simulating power electronics systems: PLECS (Piecewise Linear Electrical Circuit Simulation) [31]. The PLECS implementation of the considered MMC is reported in Fig. 3, in which the case $n = 3$ has been taken as an example. Since the objective is the verification of the proposed model (5), the simulation of the system model (5) and the simulation of the PLECS model have been performed in open-loop by applying the same control signals T_1, \dots, T_6 in vectors \mathbf{T}_1 and \mathbf{T}_2 in (4). The considered model parameters and initial conditions are reported in Table 1.

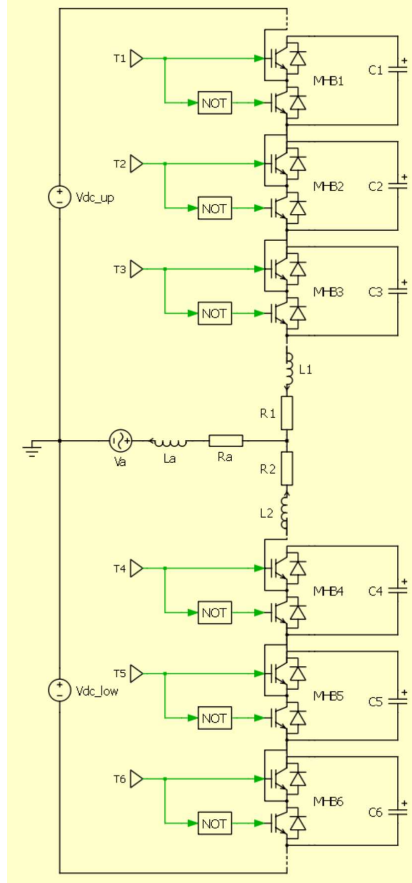


Figure 3: PLECS implementation of the MMC circuit diagram in Fig. 1 for the case $n = 3$.

The results in terms of currents I_1 and I_2 , voltages V_1 and V_2 and capacitor voltages V_{c_1}, \dots, V_{c_6} given by the PLECS model in Fig. 3 are shown in the PLECS scopes in Fig. 4. The comparison between the results given by the model (5) and those given by the PLECS model are reported in Fig. 5. In this figure, the legend notation “PI” stands for PLECS and “Mt” stands for Matlab/Simulink. From Fig. 5, it is possible to appreciate the very good superposition between the results of model (5) and those given the PLECS model in Fig. 3. In fact, the maximum absolute difference between the capacitor voltages V_{c_1}, \dots, V_{c_6} given by the simulation of the PLECS model and those given by the simulation of model (5) is 12.5 mV, the maximum absolute difference between currents I_1, I_2 given by the simulation of the PLECS model and those given by the simulation of model (5) is 14.2 mA, and the

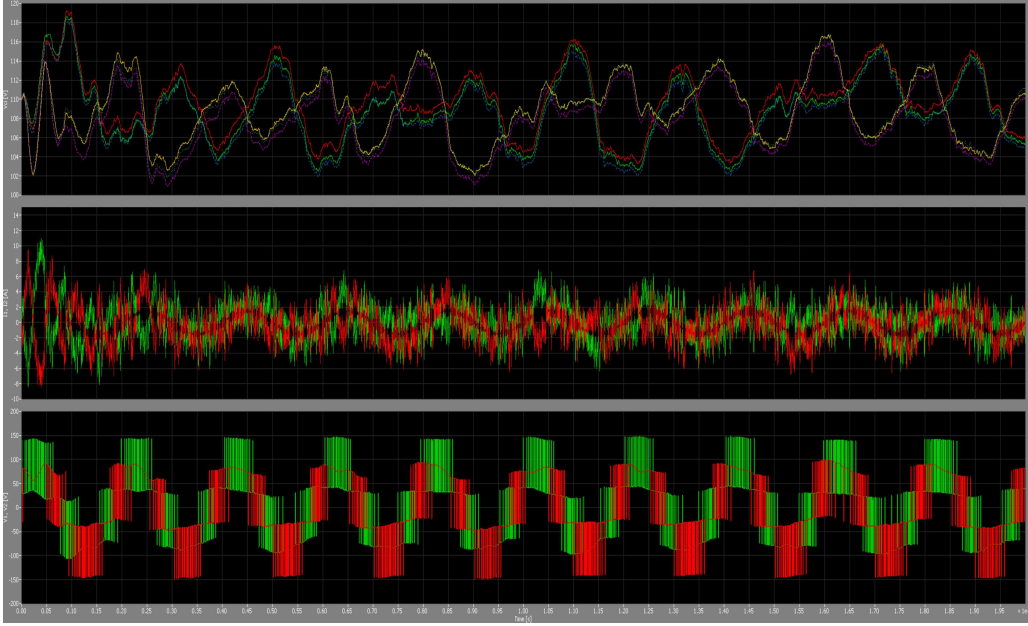


Figure 4: Capacitor voltages V_{c_1}, \dots, V_{c_6} , currents I_1, I_2 and voltages V_1, V_2 given by the PLECS scope.

maximum absolute difference between voltages V_1, V_2 given by the simulation of the PLECS model and those given by the simulation of model (5) is 31.66 mV. This verifies the correctness of the MMC model proposed in (5).

2.3. Average dynamic model of the MMC capacitive part

The order of the capacitive part (2)-(4) in the MMC dynamic model is $2n$, that is the total number of capacitors in the upper and lower arms of the converter. Let C be the capacitance value of capacitors $C_1, \dots, C_n, C_{n+1}, \dots, C_{2n}$ in the MMC of Fig. 1. In order to have equally spaced voltage levels for voltages V_1 and V_2 , see Fig. 1, the following balancing conditions must stand:

$$V_{c_1} \simeq \dots \simeq V_{c_n} \simeq \bar{V}_{c_1}, \quad V_{c_{n+1}} \simeq \dots \simeq V_{c_{2n}} \simeq \bar{V}_{c_2}, \quad (6)$$

where \bar{V}_{c_1} and \bar{V}_{c_2} are the average values of the capacitors voltages in the upper and lower arms of the converter, respectively. Condition (6) can be effectively achieved using the algorithm described in Sec. 3.1. If (6) holds true, the dynamic model of the MMC capacitive part can be approximated using the following average dynamic model. Let $\bar{\mathbf{V}}_c$ denote the following

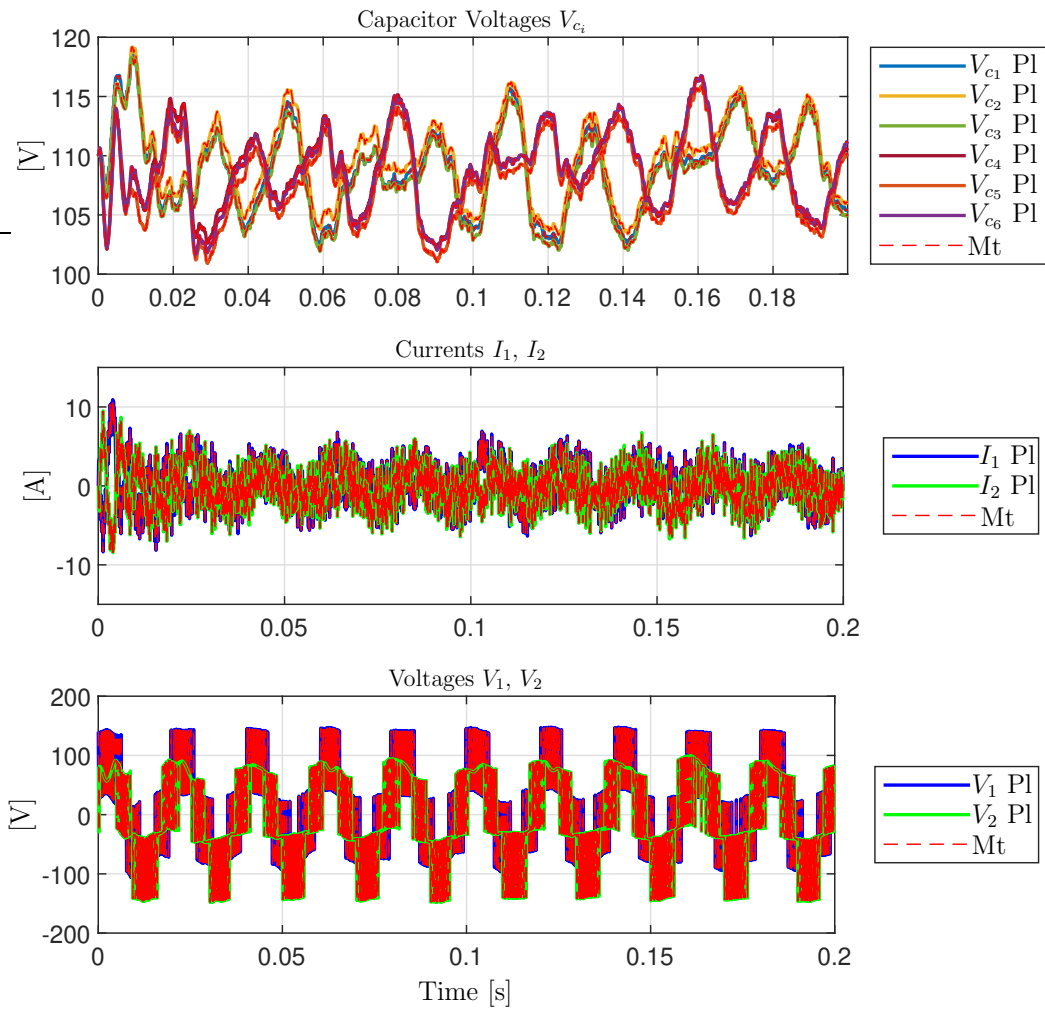


Figure 5: Comparison between Matlab/Simulink and PLECS results: capacitor voltages V_{c_i} , currents I_1, I_2 and voltages V_1, V_2 .

vector:

$$\bar{\mathbf{V}}_c = \begin{bmatrix} \bar{V}_{c1} \\ \bar{V}_{c2} \end{bmatrix}. \quad (7)$$

The variables V_1 and V_2 of vector \mathbf{V}_C in (1) can only take on the following admissible voltage values:

$$\mathbf{V}_C = \begin{bmatrix} V_1 \\ V_2 \end{bmatrix} = \begin{bmatrix} V_{dc} - n_1 \bar{V}_{c1} \\ -V_{dc} + n_2 \bar{V}_{c2} \end{bmatrix}, \quad (8)$$

where the integers $n_1 \in \{0, 1, 2, \dots, n\}$ and $n_2 \in \{0, 1, 2, \dots, n\}$ denote the number of capacitors for which the corresponding switch is off in the upper and lower arms of the converter, i.e. for which $T_i = 1$ in Fig. 1. The time derivative of the average voltage vector $\bar{\mathbf{V}}_c$ in (7) can be expressed as follows:

$$\dot{\bar{\mathbf{V}}}_c = \begin{bmatrix} \frac{d\bar{V}_{c1}}{dt} \\ \frac{d\bar{V}_{c2}}{dt} \end{bmatrix} = \begin{bmatrix} \frac{n_1 I_1}{n C} \\ -\frac{n_2 I_2}{n C} \end{bmatrix} = \frac{1}{C_T} \begin{bmatrix} n_1 I_1 \\ -n_2 I_2 \end{bmatrix}, \quad (9)$$

where $C_T = n C$. Using (8) and (9), the dynamic model of the MMC can be expressed as $\mathbf{L}_s \dot{\mathbf{x}}_s = \mathbf{A}_s \mathbf{x}_s + \mathbf{B}_s \mathbf{u}$:

$$\underbrace{\begin{bmatrix} \mathbf{C}_T & \mathbf{0} \\ \mathbf{0} & \mathbf{L}_L \end{bmatrix}}_{\mathbf{L}_s} \dot{\mathbf{x}}_s = \underbrace{\begin{bmatrix} \mathbf{0} & \mathbf{A}_{12} \\ -\mathbf{A}_{12}^T & \mathbf{A}_L \end{bmatrix}}_{\mathbf{A}_s} \underbrace{\begin{bmatrix} \bar{\mathbf{V}}_c \\ \mathbf{I}_L \end{bmatrix}}_{\mathbf{x}_s} + \underbrace{\begin{bmatrix} \mathbf{0} & \mathbf{0} \\ \mathbf{d}_c & \mathbf{b}_L \end{bmatrix}}_{\mathbf{B}_s} \underbrace{\begin{bmatrix} V_{dc} \\ V_a \end{bmatrix}}_{\mathbf{u}}, \quad \mathbf{C}_T = \begin{bmatrix} C_T & 0 \\ 0 & C_T \end{bmatrix}, \quad \mathbf{A}_{12} = \begin{bmatrix} n_1 & 0 \\ 0 & -n_2 \end{bmatrix}. \quad (10)$$

2.4. Transformed average model of the MMC

Applying the following transformations:

$$\underbrace{\begin{bmatrix} I_1 \\ I_2 \end{bmatrix}}_{\mathbf{I}_L} = \frac{1}{2} \underbrace{\begin{bmatrix} 1 & 1 \\ 1 & -1 \end{bmatrix}}_{\mathbf{T}_w} \underbrace{\begin{bmatrix} I_s \\ I_d \end{bmatrix}}_{\mathbf{I}_w}, \quad \underbrace{\begin{bmatrix} V_1 \\ V_2 \end{bmatrix}}_{\mathbf{V}_C} = \frac{1}{2} \underbrace{\begin{bmatrix} 1 & 1 \\ 1 & -1 \end{bmatrix}}_{\mathbf{T}_w} \underbrace{\begin{bmatrix} V_s \\ V_d \end{bmatrix}}_{\mathbf{V}_w}. \quad (11)$$

to the inductive part (1) of the MMC complete model, one obtains:

$$\underbrace{\frac{1}{4} \begin{bmatrix} 2L+4L_a & 0 \\ 0 & 2L \end{bmatrix}}_{\mathbf{L}_w} \dot{\mathbf{i}}_w = -\underbrace{\frac{1}{4} \begin{bmatrix} 2R+4R_a & 0 \\ 0 & 2R \end{bmatrix}}_{\mathbf{A}_w} \underbrace{\begin{bmatrix} I_s \\ I_d \end{bmatrix}}_{\mathbf{I}_w} + \underbrace{\frac{1}{2} \begin{bmatrix} V_s \\ V_d \end{bmatrix}}_{\mathbf{V}_w} + \underbrace{\begin{bmatrix} -1 \\ 0 \end{bmatrix}}_{\mathbf{b}_w} V_a, \quad (12)$$

where $\mathbf{L}_w = \mathbf{T}_w^T \mathbf{L}_L \mathbf{T}_w$, $\mathbf{A}_w = \mathbf{T}_w^T \mathbf{A}_L \mathbf{T}_w$, $\mathbf{V}_w = \mathbf{T}_w^T \mathbf{V}_C$ and $\mathbf{b}_w = \mathbf{T}_w^T \mathbf{b}_L$, see [25]. Note that variable I_s is (11) is the load current I_a , by applying

the Kirchhoff's Current Law to the circuit diagram in Fig. 1. Hereinafter, variable I_s will be used to denote the load current I_a . The two equations of system (12) can be expanded as follows:

$$\begin{cases} L_T \dot{I}_s = -R_T I_s - 2V_a + V_s \\ L \dot{I}_d = -R I_d + V_d \end{cases}, \quad (13)$$

where $L_T = L + 2L_a$ and $R_T = R + 2R_a$. System (13) can be controlled by using the input voltages V_s and V_d introduced in (11). An important observation has to be made on system (13): the dynamics of currents I_s and I_d are *decoupled*: current I_s can only be controlled by using the input voltage V_s , see the first equation of system (13), whereas current I_d can only be controlled by using the input voltage V_d , see the second equation of system (13). By replacing current I_s in (13) with the desired one \tilde{I}_a , one obtains the desired value \tilde{V}_s of voltage V_s :

$$\tilde{V}_s = f(t) = L_T \dot{\tilde{I}}_a + R_T \tilde{I}_a + 2V_a. \quad (14)$$

Inverting (8), the control variables n_1 and n_2 can be expressed as follows:

$$\begin{bmatrix} n_1 \\ n_2 \end{bmatrix} = \begin{bmatrix} \frac{V_{dc} - V_1}{\bar{V}_{c1}} \\ \frac{V_{dc} + V_2}{\bar{V}_{c2}} \end{bmatrix}. \quad (15)$$

Substituting (15) in (9), one obtains the following nonlinear dynamic equations describing the capacitive part of the MMC:

$$\begin{cases} C_T \bar{V}_{c1} \dot{\bar{V}}_{c1} = (V_{dc} - V_1) I_1 \\ C_T \bar{V}_{c2} \dot{\bar{V}}_{c2} = -(V_{dc} + V_2) I_2 \end{cases}. \quad (16)$$

Applying the transformations in (11) to system (16), one obtains:

$$\begin{cases} 4C_T \bar{V}_{c1} \dot{\bar{V}}_{c1} = (2V_{dc} - V_s - V_d)(I_s + I_d) \\ 4C_T \bar{V}_{c2} \dot{\bar{V}}_{c2} = -(2V_{dc} + V_s - V_d)(I_s - I_d) \end{cases}. \quad (17)$$

The overall dynamic equations of the transformed average MMC model are given by combining together the transformed equations (13) and (17) of the inductive and capacitive parts of the system, respectively.

3. Model-Based Adaptive Control of Modular Multilevel Converters

Control Problem. Let $\tilde{I}_a = I_{aM} \sin(\omega t)$ be the desired load current, and let $V_a = V_{aM} \sin(\omega t + \alpha_{V_a})$ be the load generator voltage source in Fig. 1. The control Goals are:

1) Capacitor voltages control: 1.1) Keeping $V_{c_1} \simeq \dots \simeq V_{c_n} \simeq \bar{V}_{c_1}$ and $V_{c_{n+1}} \simeq \dots \simeq V_{c_{2n}} \simeq \bar{V}_{c_2}$ (capacitor voltages balancing); 1.2) Keeping $\bar{V}_{c_1} \simeq \bar{V}_{c_2} \simeq \bar{V}_{c_{12_{des}}}$, where $\bar{V}_{c_{12_{des}}}$ is the optimal average capacitor voltages reference, which in turn translates into the definition of a desired profile \tilde{I}_d for current I_d .

2) Load current control: the load current I_s must track the desired profile \tilde{I}_a ;

The solution of Goal 1.1 of the Control Problem, that is the capacitor voltages balancing problem, is addressed in Sec. 3.1. In Sec. 3.2, the transformed average MMC model in (13) and (17) is properly linearized. The harmonic analysis performed in Sec. 3.2.1 on the linearized model allows to determine the algorithm to compute the desired current profile \tilde{I}_d in Sec. 3.2.2, on the basis of the optimal average capacitor voltages reference $\bar{V}_{c_{12_{des}}}$ computed in Sec. 3.2.3. Finally, the optimal control solving Goals 1.2 and 2 of the Control Problem is discussed in Sec. 3.3.

3.1. Solution of Goal 1.1 of the Control Problem

Recalling that n is the number of capacitors in the upper and lower arms of the MMC, let $i \in \{1, \dots, n\}$ and $j \in \{1, 2\}$ be the indexes identifying the $(i + (j - 1) \times n)$ -th capacitor voltage $V_{c_{i+(j-1) \times n}}$, where $j = 1$ identifies the upper MMC arm and $j = 2$ identifies the lower MMC arm, see Fig. 1. The Goal 1.1 of the Control Problem in Sec. 3 is achieved by implementing the algorithm schematized in Fig. 6. The algorithm takes as input: the index j identifying the MMC arm under consideration, the arm current I_j (see (1)), the capacitor voltages vector \mathbf{V}_{c_j} (see (3)) and the index n_j defining the desired level for voltage V_j in the considered arm $j \in \{1, 2\}$ (see (8)). The indexes n_j are the solution of the optimization problem (40) described in Sec. 3.3.1. The algorithm in Fig. 6 generates as output the control vector \mathbf{T}_j in the considered arm j (see (3)), and works as follows. If $j = 1$, according to the sign notations adopted in Fig. 1, a positive current $I_1 > 0$ recharges the capacitors C_i in the upper arm for which $T_i = 1$, making the corresponding voltages V_{c_i} increase. Therefore, if $j = 1$ and $I_1 > 0$, T_i is set to 1 for the

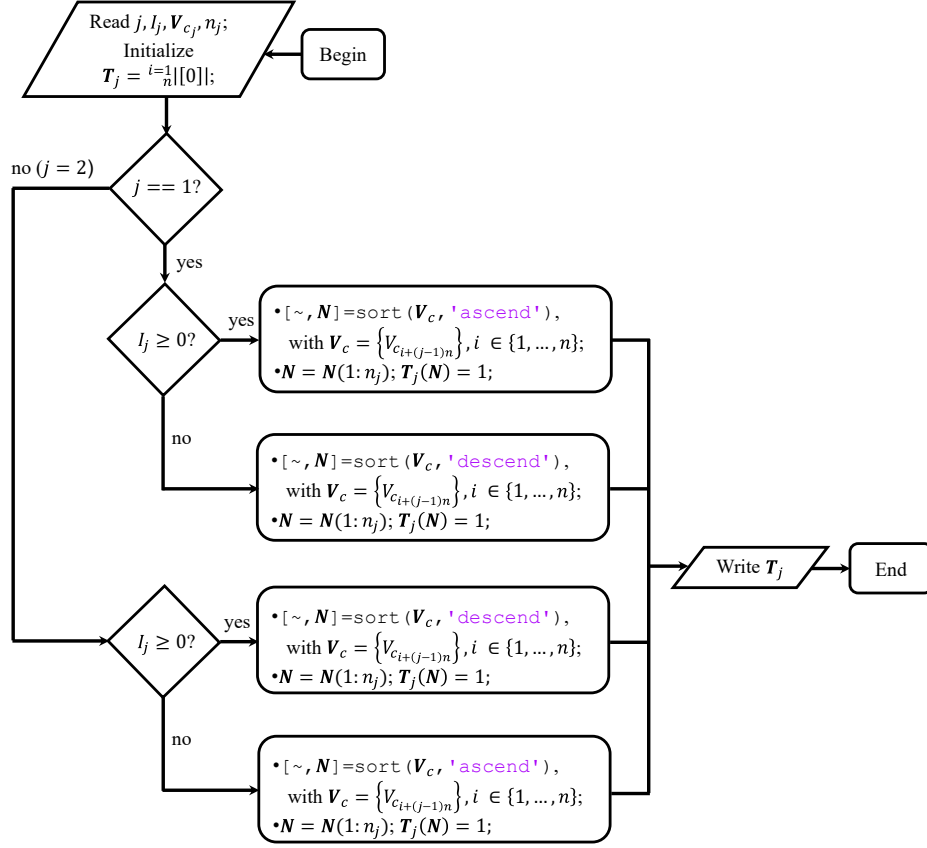


Figure 6: Algorithm solving Goal 1.1 of the Control Problem in Sec. 3.

n_1 capacitors having the lowest voltages V_{c_i} , where n_1 identifies the required number of capacitors to be connected in order to generate the desired voltage level V_1 in the upper arm according to (8). Conversely, if $j = 1$ and $I_1 < 0$, T_i is set to 1 for the n_1 capacitors having the highest voltages V_{c_i} . In doing so, the control vector \mathbf{T}_1 in (3) is determined. If $j = 2$, according to the sign notations adopted in Fig. 1, a positive current $I_2 > 0$ discharges the capacitors C_i in the upper arm for which $T_i = 1$, making the corresponding voltages V_{c_i} increase. Therefore, the logic for sorting the capacitors to be activated is opposite with respect to the upper arm $j = 1$, in order to determine the control vector \mathbf{T}_2 in (3).

3.2. Calculation of the desired current profile \tilde{I}_d

Substituting $I_s = \tilde{I}_a$ and \tilde{V}_s given in (14) in the second equation of (13) and in (17), one obtains the following set of differential equations:

$$\begin{cases} L \dot{I}_d = -R I_d + V_d \\ 4 C_T \bar{V}_{c1} \dot{\bar{V}}_{c1} = [2 V_{dc} - V_d - f(t)] (I_d + \tilde{I}_a) \\ 4 C_T \bar{V}_{c2} \dot{\bar{V}}_{c2} = [2 V_{dc} - V_d + f(t)] (I_d - \tilde{I}_a) \end{cases} \quad (18)$$

Note: the last two equations of system (18) are nonlinear with respect to variables \bar{V}_{c1} and \bar{V}_{c2} . By introducing the substitutions $2 \bar{V}_{c1} \dot{\bar{V}}_{c1} = \dot{\bar{V}}_{c1}^2$ and $2 \bar{V}_{c2} \dot{\bar{V}}_{c2} = \dot{\bar{V}}_{c2}^2$ in system (18), and expanding the right part, one can rewrite the system in the following form:

$$\begin{cases} L \dot{I}_d = -R I_d + V_d, \\ 2 C_T \dot{\bar{V}}_{c1}^2 = P_1(t) + P_2(t), \\ 2 C_T \dot{\bar{V}}_{c2}^2 = P_1(t) - P_2(t), \end{cases} \quad \text{where} \quad \begin{cases} P_1(t) = 2 V_{dc} I_d - V_d I_d - f(t) \tilde{I}_a, \\ P_2(t) = 2 V_{dc} \tilde{I}_a - V_d \tilde{I}_a - f(t) I_d. \end{cases} \quad (19)$$

The last two equations of (19) are now linear with respect to variables \bar{V}_{c1}^2 and \bar{V}_{c2}^2 . From (19), it is also evident that: a) when $P_1(t)$ is positive, both voltages \bar{V}_{c1} and \bar{V}_{c2} increase; when $P_1(t)$ is negative, both voltages \bar{V}_{c1} and \bar{V}_{c2} decrease. This means that function $P_1(t)$ can be used to make the two voltages \bar{V}_{c1} and \bar{V}_{c2} follow the optimal average capacitor voltages reference \bar{V}_{c12des} . b) when $P_2(t)$ is positive, voltage \bar{V}_{c1} increases and voltage \bar{V}_{c2} decreases; when $P_2(t)$ is negative, voltage \bar{V}_{c1} decreases and voltage \bar{V}_{c2} increases. This means that function $P_2(t)$ can be used to enforce the condition $\bar{V}_{c1} \simeq \bar{V}_{c2}$.

3.2.1. Harmonic analysis of dynamic system (19)

Recalling that the desired load current \tilde{I}_a and the input voltage V_a exhibit a sinusoidal behavior as in (20), we are going to design voltage V_d to exhibit a sinusoidal behavior as well, with the addition of an offset V_{d0} as in (21):

$$\begin{aligned} \tilde{I}_a &= I_{aM} \sin(\omega t), \\ V_a &= V_{aM} \sin(\omega t + \alpha_{V_a}), \end{aligned} \quad (20) \quad \begin{aligned} V_d &= V_{d0} + V_{dM} \sin(\omega t + \alpha_{V_d}). \end{aligned} \quad (21)$$

The design of the parameters V_{d0} , V_{dM} and α_{V_d} of voltage V_d in (21) is addressed based on the following harmonic analysis.

Sinusoidal behavior of function I_d : at steady-state, when voltage V_d in (21) is applied, the solution of the first equation of system (19) is:

$$I_d = I_{d0} + I_{dM} \sin(\omega t + \alpha_{V_d} - \alpha_{LR}) \quad \text{where} \quad \begin{cases} I_{d0} = \frac{V_{d0}}{R}, \\ I_{dM} = \frac{V_{dM}}{\sqrt{R^2 + L^2 \omega^2}}, \\ \alpha_{LR} = \arctan\left(\frac{L\omega}{R}\right). \end{cases} \quad (22)$$

Sinusoidal behavior of function $P_1(t)$: It can be proven, see App. A, that function $P_1(t)$ in (19) can be written as $P_1(t) = P_{10} + P_1(\omega t)$, where:

$$\begin{cases} P_{10} = 2V_{dc}I_{d0} - V_{d0}I_{d0} - \frac{V_{dM}I_{dM}}{2} \cos(\alpha_{LR}) - \frac{f_M I_{aM}}{2} \cos(\alpha_f), \\ P_1(\omega t) = 2V_{dc}I_{dM} \sin(\omega t + \alpha_{V_d} - \alpha_{LR}) - F_{V_d} I_d(\omega t) + \frac{f_M I_{aM}}{2} \cos(2\omega t + \alpha_f). \end{cases} \quad (23)$$

Parameters f_M and α_f are defined in (A.2). Using (22), the constant term P_{10} in (23) can be expressed as:

$$P_{10} = \frac{2V_{dc}V_{d0}}{R} - \frac{V_{d0}^2}{R} - \frac{V_{dM}^2}{2\sqrt{R^2 + L^2 \omega^2}} \cos(\alpha_{LR}) - \frac{f_M I_{aM}}{2} \cos(\alpha_f) = \frac{2V_{dc}V_{d0} - V_{d0}^2 - C_0}{R}, \quad (24)$$

where parameter C_0 is defined as follows:

$$C_0 = \frac{R V_{dM}^2}{2\sqrt{R^2 + L^2 \omega^2}} \cos(\alpha_{LR}) + \frac{R f_M I_{aM}}{2} \cos(\alpha_f). \quad (25)$$

From (24), one can verify that term P_{10} is positive if:

$$V_{d0}^- = V_{dc} - \sqrt{V_{dc}^2 - C_0} < V_{d0} < V_{dc} + \sqrt{V_{dc}^2 - C_0}. \quad (26)$$

Sinusoidal behavior of function $P_2(t)$: It can be proven, see App. C, that function $P_2(t)$ in (19) can be written as $P_2(t) = P_{20} + P_2(\omega t)$, where:

$$\begin{cases} P_{20} = -\frac{V_{dM} I_{aM}}{2} \cos(\alpha_{V_d}) - \frac{f_M I_{dM}}{2} \cos(\alpha_f - \alpha_{V_d} + \alpha_{LR}), \\ P_2(\omega t) = 2V_{dc} I_{aM} \sin(\omega t) - F_2(\omega t) - F_3(\omega t). \end{cases} \quad (27)$$

The sinusoidal functions $F_2(\omega t)$ and $F_3(\omega t)$ are defined in App. C. After some elaboration, see App. F, the constant term P_{20} can be written as:

$$P_{20} = -\frac{V_{dM} \sqrt{a^2 + b^2}}{2} \cos(\alpha_{V_d} + \gamma), \quad a = I_{aM} + \frac{f_M \cos(\beta)}{\sqrt{R^2 + L^2 \omega^2}}, \quad b = \frac{f_M \sin(\beta)}{\sqrt{R^2 + L^2 \omega^2}}, \quad (28)$$

where $\beta = -\alpha_f - \alpha_{LR}$ and $\gamma = \arctan2(b, a)$. The values of parameters f_M , α_f and α_{LR} are given in (A.2) and (22).

Using (23) and (27), system (19) can be rewritten as follows:

$$\begin{cases} L \dot{I}_d = -R I_d + V_d \\ 2 C_T \dot{\bar{V}}_{c1}^2 = P_{10} + P_{20} + P_1(\omega t) + P_2(\omega t) \\ 2 C_T \dot{\bar{V}}_{c2}^2 = P_{10} - P_{20} + P_1(\omega t) - P_2(\omega t) \end{cases} . \quad (29)$$

The terms $P_1(\omega t)$ and $P_2(\omega t)$ in (29) are the sum of sinusoidal functions at frequency ω and 2ω with zero average value. Therefore, they produce a periodic oscillation on variables \bar{V}_{c1}^2 and \bar{V}_{c2}^2 at steady-state, but they do not modify their average values. It follows that the average values of the two variables \bar{V}_{c1}^2 and \bar{V}_{c2}^2 can only be modified by the two constant terms P_{10} and P_{20} .

3.2.2. Algorithm computing the desired current profile \tilde{I}_d

Observation 1): choosing the value $\alpha_{V_d} = -\gamma$ for the design parameter α_{V_d} , the expression of constant term P_{20} in (28) simplifies as follows:

$$P_{20} = -\frac{V_{dM} \sqrt{a^2 + b^2}}{2}. \quad (30)$$

From (30), it is clear that parameter V_{dM} directly affects the value of the constant term P_{20} . Specifically, the design parameter V_{dM} has the following impact on term P_{20} and, consequently, on variables \bar{V}_{c1} and \bar{V}_{c2} :

$$\begin{cases} V_{dM} > 0 \leftrightarrow P_{20} < 0 \leftrightarrow (\bar{V}_{c1} \downarrow) \wedge (\bar{V}_{c2} \uparrow) \\ V_{dM} < 0 \leftrightarrow P_{20} > 0 \leftrightarrow (\bar{V}_{c1} \uparrow) \wedge (\bar{V}_{c2} \downarrow) \end{cases}, \quad (31)$$

where \downarrow and \uparrow denote a decreasing and an increasing variation of the variable next to the arrow. Parameter V_{dM} can therefore be effectively exploited to enforce the condition $\bar{V}_{c1} \simeq \bar{V}_{c2}$.

Observation 2): the design parameter V_{d0} in (21) can be effectively exploited in order to make the two voltages \bar{V}_{c1} and \bar{V}_{c2} track the optimal average capacitor voltages reference $\bar{V}_{c12_{des}}$. Once the parameters V_{dM} and α_{V_d} have been chosen as described in 1) in order to enforce $\bar{V}_{c1} \simeq \bar{V}_{c2}$, and using P_{10} in (24) and C_0 in (25), the design parameter V_{d0} has the following impact on term P_{10} and on variables \bar{V}_{c1} and \bar{V}_{c2} , see (24), (26) and (29):

$$\begin{cases} V_{d0} > V_{d0}^- \leftrightarrow P_{10} > 0 \leftrightarrow (\bar{V}_{c1} \uparrow) \wedge (\bar{V}_{c2} \uparrow) \\ V_{d0} < V_{d0}^- \leftrightarrow P_{10} < 0 \leftrightarrow (\bar{V}_{c1} \downarrow) \wedge (\bar{V}_{c2} \downarrow) \end{cases}, \quad (32)$$

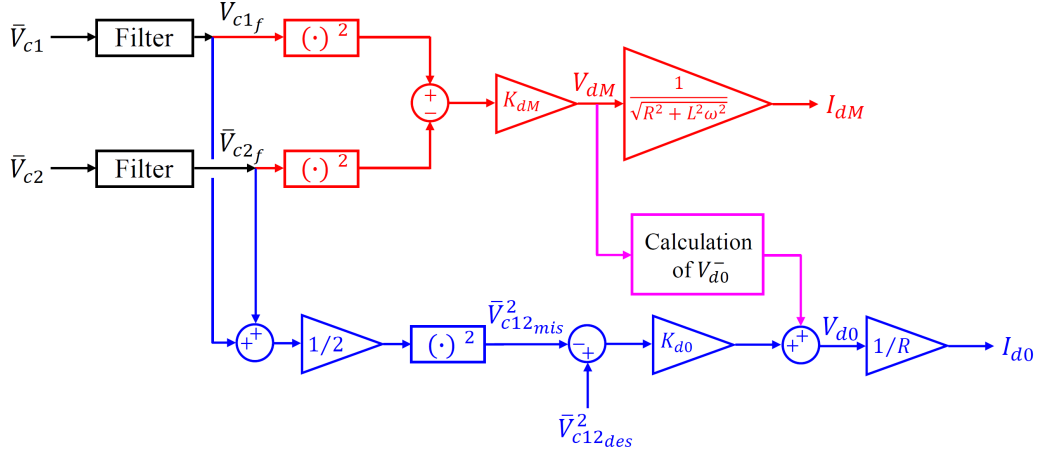


Figure 7: Algorithm for the generation of parameters I_{d0} and I_{dM} of the desired current \tilde{I}_d .

In fact, the constant term P_{10} is positive if parameter V_{d0} belongs to the range defined in (26). Parameter V_{d0} can therefore be effectively exploited to increase or decrease the value of both voltages \bar{V}_{c1} and \bar{V}_{c2} , in order to make track follow the optimal average capacitor voltages reference \bar{V}_{c12des} .

Based on the observations 1) and 2) reported above, the parameters I_{d0} and I_{dM} of the desired current profile \tilde{I}_d having the form described in (22) are computed using the algorithm reported in Fig. 7 consisting in two control loops, where the first loop affects the second one.

Loop 1: The first loop, highlighted in red in Fig. 7, computes:

$$I_{dM} = \frac{V_{dM}}{\sqrt{R^2 + L^2 \omega^2}} = \frac{K_{dM}}{\sqrt{R^2 + L^2 \omega^2}} (\bar{V}_{c1f}^2 - \bar{V}_{c2f}^2), \quad (33)$$

where \bar{V}_{c1f} and \bar{V}_{c2f} are a filtered version of the voltages \bar{V}_{c1} and \bar{V}_{c2} . This control law, based on the choice $\alpha_{V_d} = -\gamma$, provides the value of the design parameter I_{dM} in order to enforce $\bar{V}_{c1} \simeq \bar{V}_{c2}$, and is based on relations (31) and (22).

Loop 2: The second loop, highlighted in blue in Fig. 7, computes:

$$I_{d0} = \frac{V_{d0}}{R} = \frac{V_{d0}^- + K_{d0}(\bar{V}_{c12des}^2 - \bar{V}_{c12mis}^2)}{R}, \quad \bar{V}_{c12mis} = \frac{\bar{V}_{c1f} + \bar{V}_{c2f}}{2}, \quad (34)$$

where V_{d0}^- is the threshold given in (26), \bar{V}_{c12mis} is the measured mean value

of voltages \bar{V}_{c1f} and \bar{V}_{c2f} , and \bar{V}_{c12des} is the optimal reference of the average capacitor voltages \bar{V}_{c1} and \bar{V}_{c2} . Note that the error considered in (34) is $\bar{V}_{c12des}^2 - \bar{V}_{c12mis}^2$ instead of $\bar{V}_{c12des} - \bar{V}_{c12mis}$; this is because system (19) is linear with respect to variables \bar{V}_{c1f}^2 and \bar{V}_{c2f}^2 . The control law in (34) provides the value of the design parameter I_{d0} in order to maintain the mean value \bar{V}_{c12mis} track the optimal reference \bar{V}_{c12des} exploiting relations (32).

The part highlighted in magenta in Fig. 7 represents the calculation of parameter $V_{d0}^- = V_{d0}^-(V_{dM})$ according to (25), (26) and using the control parameter V_{dM} generated by the first control loop (red one in Fig. 7). The quantity $V_{d0}^- = V_{d0}^-(V_{dM})$ is then injected into the second control loop (blue one in Fig. 7).

3.2.3. Optimal average capacitor voltages reference \bar{V}_{c12des}

On one hand, (8) shows that smaller values for voltages \bar{V}_{c1} and \bar{V}_{c2} allow to obtain discrete voltage levels for V_1 and V_2 which are closer to each other, thus reducing their harmonic content as well as the harmonic content of the generated load current I_s through (2), (3) and recalling that $I_s = I_a = I_1 + I_2$, see Fig. 1. This significantly enhances the main intrinsic advantages of multilevel converters. On the other hand, from (8) it is clear that small values for voltages \bar{V}_{c1} and \bar{V}_{c2} limit the lower boundary of voltage V_1 and the upper boundary of voltage V_2 . This may compromise the generation of currents I_1 and I_2 in the complete MMC system since the condition (14) may not be satisfied, given that $V_s = V_1 + V_2$. The amplitude I_{aM} and the frequency ω of the desired load current $\tilde{I}_a = \tilde{I}_a(t)$ given in (20) can be, in general, time-variant due to variations of the operating conditions, such as a fault for example, leading to variations of the desired voltage \tilde{V}_s through (14). Using the desired \tilde{I}_d from the algorithm in Fig. 7 and the first equation in (29), one obtains the desired reference \tilde{V}_d for voltage V_d . From \tilde{V}_d , \tilde{V}_s in (14) and using (11), one obtains the desired references \tilde{V}_1 and \tilde{V}_2 for voltages V_1 and V_2 :

$$\tilde{V}_1 = \frac{\tilde{V}_s + V_d}{2} \quad \text{and} \quad \tilde{V}_2 = \frac{\tilde{V}_s - V_d}{2}. \quad (35)$$

Let \tilde{V}_{1M} and \tilde{V}_{2M} denote the maximum values of the two desired voltages \tilde{V}_1 and \tilde{V}_2 , and let $\tilde{V}_{12M} = (\tilde{V}_{1M} + \tilde{V}_{2M})/2$. Since $\tilde{V}_{1M} \simeq \tilde{V}_{2M}$ is desired, then $\tilde{V}_{12M} \simeq \tilde{V}_{1M} \simeq \tilde{V}_{2M}$. The optimal voltage reference \bar{V}_{c12des} used in the control scheme of Fig. 7 can be obtained, for example, from the second equation in

(8) when the desired voltage \tilde{V}_2 takes on its maximum value \tilde{V}_{12M} (i.e. when $n_2 = n$):

$$\bar{V}_{c12des} = \frac{\tilde{V}_{12M} + V_{dc}}{n}. \quad (36)$$

3.3. Solution of Goals 1.2 and 2 of the Control Problem

The inductive part of the MMC model in (1) can be rewritten as:

$$\begin{bmatrix} \dot{I}_1 \\ \dot{I}_2 \end{bmatrix} = \mathbf{L}_L^{-1} \mathbf{A}_L \begin{bmatrix} I_1 \\ I_2 \end{bmatrix} + \mathbf{L}_L^{-1} \begin{bmatrix} V_1 - V_a \\ V_2 - V_a \end{bmatrix}. \quad (37)$$

Let $I_1(k)$, $I_2(k)$ and $I_1(k+1)$, $I_2(k+1)$ be the values of currents I_1 and I_2 at the discrete time instants $t = kT_s$ and $t = (k+1)T_s$, where T_s is the sampling time. Recalling the definition of incremental ratio, one can write:

$$\dot{I}_1 \approx \frac{I_1(k+1) - I_1(k)}{T_s}, \quad \dot{I}_2 \approx \frac{I_2(k+1) - I_2(k)}{T_s}. \quad (38)$$

Replacing (38) in (37), one can discretize system (37) using the Euler's forward method as follows:

$$\begin{bmatrix} I_1(k+1) \\ I_2(k+1) \end{bmatrix} = \begin{bmatrix} I_1(k) \\ I_2(k) \end{bmatrix} + \mathbf{L}_L^{-1} \mathbf{A}_L \begin{bmatrix} I_1(k) \\ I_2(k) \end{bmatrix} T_s + \mathbf{L}_L^{-1} \begin{bmatrix} V_1(k) - V_a(k) \\ V_2(k) - V_a(k) \end{bmatrix} T_s, \quad (39)$$

where $V_1(k)$, $V_2(k)$ and $V_a(k)$ are the values of voltages V_1 , V_2 and V_a at $t = kT_s$.

3.3.1. Optimal Control Problem on Currents I_a and I_d

The output of the optimal control problem shown in Fig. 8 are the optimal indexes $n_1 = n_{1opt}(k)$ and $n_2 = n_{2opt}(k)$ to be fed to the algorithm in Fig. 6 described in Sec. 3.1. Let $n_1(k-1)$ and $n_2(k-1)$ be the optimal indexes given by the optimal control at the previous time step, in order to generate the voltage levels $V_1(k-1)$ and $V_2(k-1)$ according to (8), and let w_n be a window parameter that can take on discrete values from the set $\{0, \dots, n\}$. The indexes $n_1(k)$ and $n_2(k)$ can take on values such that $n_1 \in \{n_1(k-1) - w_n, \dots, n_1(k-1) + w_n\}$ and $n_2 \in \{n_2(k-1) - w_n, \dots, n_2(k-1) + w_n\}$. Note that decreasing the window w_n has the following consequences: 1) the maximum step between two consecutive voltage levels is decreased, thus emphasizing the intrinsic advantages of multilevel converters; 2) there are fewer values of $n_1(k)$ and $n_2(k)$ to choose from for the current control

step, thus reducing the computational burden. Two nested “for” cycles are implemented over the possible values of $n_1(k)$ and $n_2(k)$, predicting the future errors $e_{I_a}(k+1)$ and $e_{I_d}(k+1)$ between the desired and actual load currents $\tilde{I}_a(k+1)$ and $I_s(k+1)$ and between the desired and actual circulating currents $\tilde{I}_d(k+1)$ and $I_d(k+1)$. These predictions are made for each admissible value of $n_1(k)$ and $n_2(k)$, as depicted by the pseudo-code reported in Fig. 8.

1.	for $n_1(k) = n_1(k-1) - w_n : n_1(k-1) + w_n$	% cycle n_1
2.	for $n_2(k) = n_2(k-1) - w_n : n_2(k-1) + w_n$	% cycle n_2
3.	$\begin{bmatrix} V_1(k) \\ V_2(k) \end{bmatrix} = \begin{bmatrix} V_{dc} - n_1(k)V_{C1}(k) \\ -V_{dc} + n_2(k)V_{C2}(k) \end{bmatrix};$	% Eq. (8)
4.	$\begin{bmatrix} I_1(k+1) \\ I_2(k+1) \end{bmatrix} = \begin{bmatrix} I_1(k) \\ I_2(k) \end{bmatrix} + \mathbf{L}_L^{-1} \mathbf{A}_L \begin{bmatrix} I_1(k) \\ I_2(k) \end{bmatrix} T_s + \mathbf{L}_L^{-1} \begin{bmatrix} V_1(k) - V_a(k) \\ V_2(k) - V_a(k) \end{bmatrix} T_s$	% Eq. (39)
5.	$I_s(k+1) = I_1(k+1) + I_2(k+1);$	% Eq. (11)
6.	$I_d(k+1) = I_1(k+1) - I_2(k+1);$	% Eq. (11)
7.	$e_{I_a}(k+1) = \tilde{I}_a(k+1) - I_s(k+1);$	
8.	$e_{I_d}(k+1) = I_{des}(k+1) - I_d(k+1);$	
9.	end	
10.	end	

Figure 8: Pseudo-code for the prediction of current errors $e_{I_a}(k+1)$ and $e_{I_d}(k+1)$.

The optimal indexes $n_{1_{opt}}(k)$ and $n_{2_{opt}}(k)$ are determined by solving the following optimal control problem:

$$\{n_{1_{opt}}(k), n_{2_{opt}}(k)\} = \min_{n_1(k), n_2(k)} (\alpha_1 e_{I_a}(k+1) + \alpha_2 e_{I_d}(k+1)), \quad (40)$$

where the two weights α_1 and α_2 composing the objective function in (40) satisfy the constraint $\alpha_1 + \alpha_2 = 1$. The optimal control problem (40) can be solved exactly thanks to the current errors prediction described in Fig. 8.

4. Simulations

Two simulations have been performed on the complete MMC system (5) using the simulink implementation in Fig. 2. The capacitor voltages balancing conditions $V_{c_1} \simeq \dots \simeq V_{c_n} \simeq \overline{V}_{c_1}$ and $V_{c_{n+1}} \simeq \dots \simeq V_{c_{2n}} \simeq \overline{V}_{c_2}$ on the

Table 2: MMC system and control parameters.

$L = 10$ [mH]	$R = 0.1$ [Ω]	$C_i = 1000$ [μ F]
$L_a = 50$ [mH]	$R_a = 19$ [Ω]	$V_a = 10 \sin(2\pi 50 t + \pi/6)$ [V]
$n = 8$	$V_{dc} = 250$ [V]	$T_s = 10^{-4}$ [s]
$I_{aM} = 1.5, 9, 0.75$ [A]	1 st order filt. $\tau = 0.0318$	$K_{d0} = 0.10 \cdot 10^{-3}$
$K_{dM} = 1.5 \cdot 10^{-3}$	$\alpha_1 = 0.99, \alpha_2 = 0.01$	$w_n = 1$

capacitor voltages in the upper and lower arms of the converter are enforced using the algorithm reported in Fig. 6 and described in Sec. 3.1, which solved the Goal 1.1 of the Control Problem in Sec. 3. The desired profile \tilde{I}_d for current I_d is generated using the scheme reported in Fig. 7. The conditions $\bar{V}_{c1} \simeq \bar{V}_{c2} \simeq \bar{V}_{c12_{des}}$ (that is $I_d \simeq \tilde{I}_d$) and $I_a \simeq \tilde{I}_a$ are achieved by solving the optimal control problem (40) in Sec. 3.3 and implementing the prediction for the future values of current errors $e_{I_d(k+1)}$ and $e_{I_a(k+1)}$ reported in Fig. 8. The MMC system and control parameters are reported in Table 2. In order to simulate changes in the system operating conditions, such as for example faults, the amplitude I_{aM} of the desired load current \tilde{I}_a has been chosen to vary as shown in the top subplot of Fig. 9, Fig. 11 and in Table 2. In the first simulation, see Fig. 9 and Fig. 10, the reference $\bar{V}_{c12_{des}}$ for the average capacitor voltages \bar{V}_{c1} and \bar{V}_{c2} is the optimal one computed as in Sec. 3.2.3. In the second simulation, see Fig. 11 and Fig. 12, the reference $\bar{V}_{c12_{des}}$ for the average capacitor voltages \bar{V}_{c1} and \bar{V}_{c2} is kept constant and equal to the minimum value which is strictly needed to follow the desired load current \tilde{I}_a during the whole simulation, which is given by the case $I_{aM} = 9$ A representing the most demanding situation. The frequency ω of the desired current \tilde{I}_a and of the input voltage V_a has been chosen to be constant and equal to $2\pi 50$ rad/s. The initial capacitor voltages are equal to 31.25 V, whereas the initial inductor currents are equal to 0 A.

First Simulation: The results of the simulation using the optimal average capacitor voltages reference $\bar{V}_{c12_{des}}$ are shown in Fig. 9 and in Fig. 10. From Fig. 9, one can observe that the reference $\bar{V}_{c12_{des}}$ for the average capacitor voltages \bar{V}_{c1} and \bar{V}_{c2} computed as in Sec. 3.2.3 is indeed the optimal one: 1) the load current I_s always follows the desired profile \tilde{I}_a as shown in the first subplot, except for very short transients when the amplitude I_{aM} changes; 2) the lower boundary $-V_{12M}$ of voltage V_1 and the upper boundary V_{12M} of voltage V_2 , computed by replacing $n_1 = n_2 = n$ in (8), always coincide with the peak value of voltages V_1 and V_2 except for the very short transients

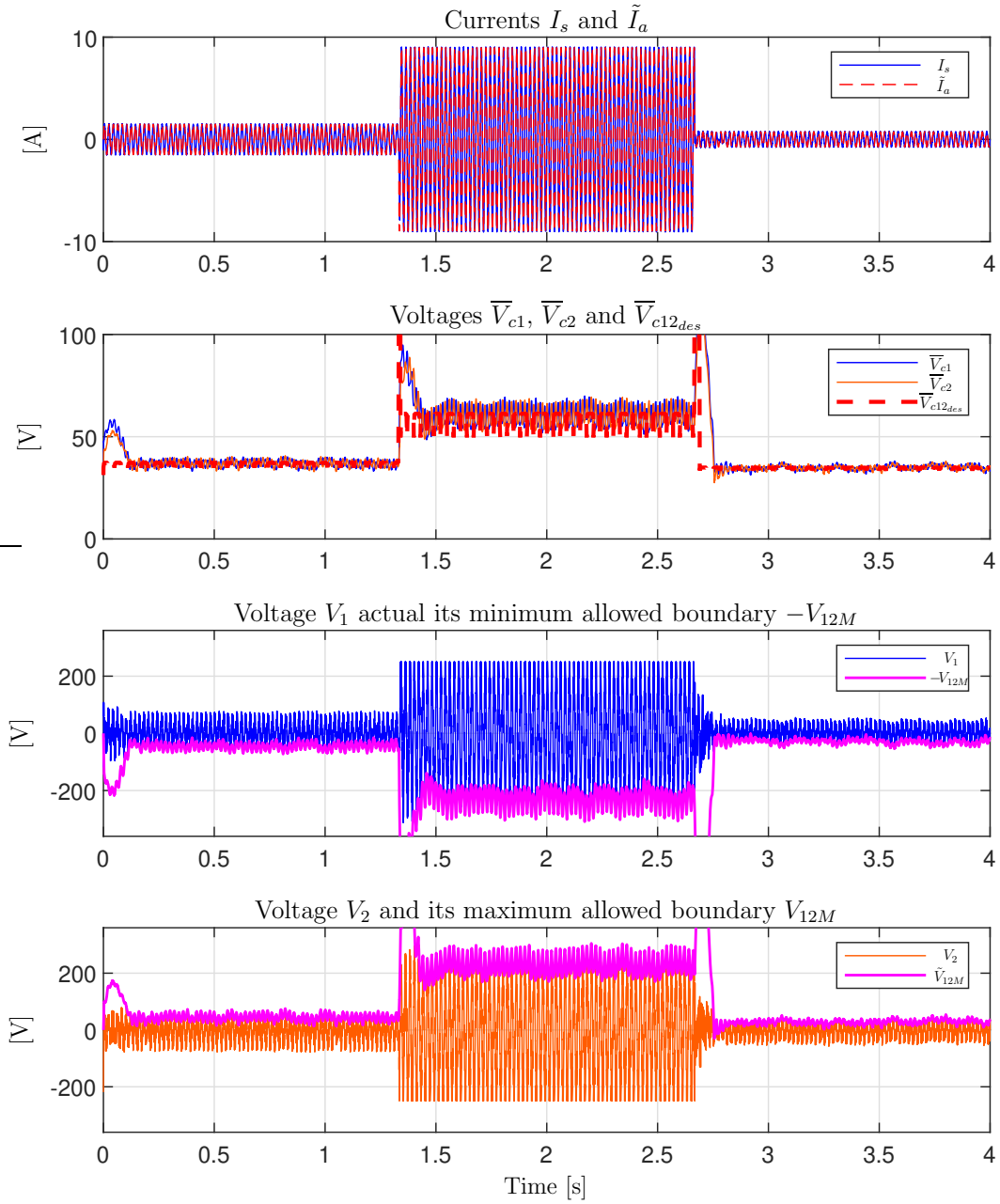


Figure 9: Results of the first simulation.

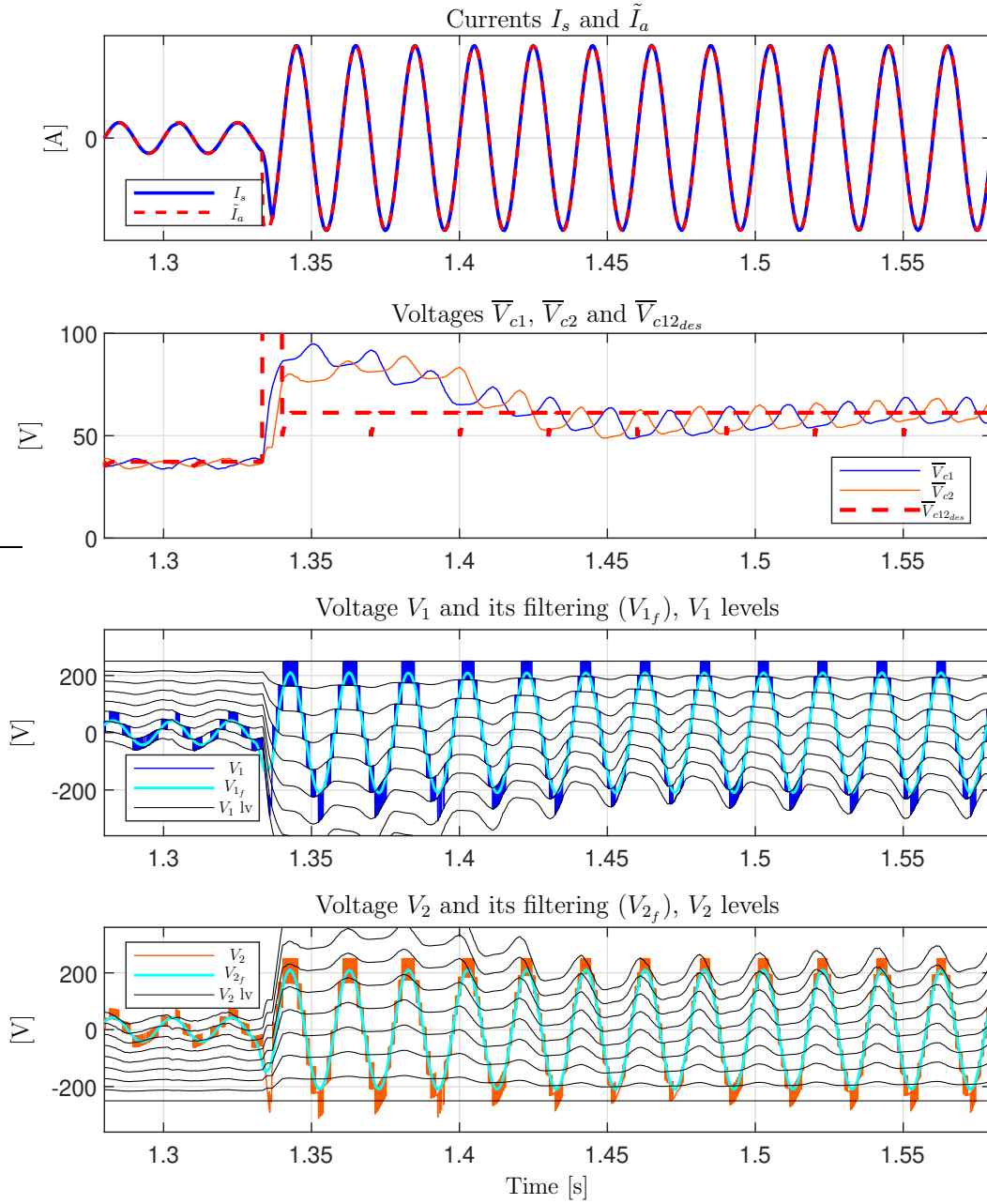


Figure 10: Results of the first simulation: zoom-in.

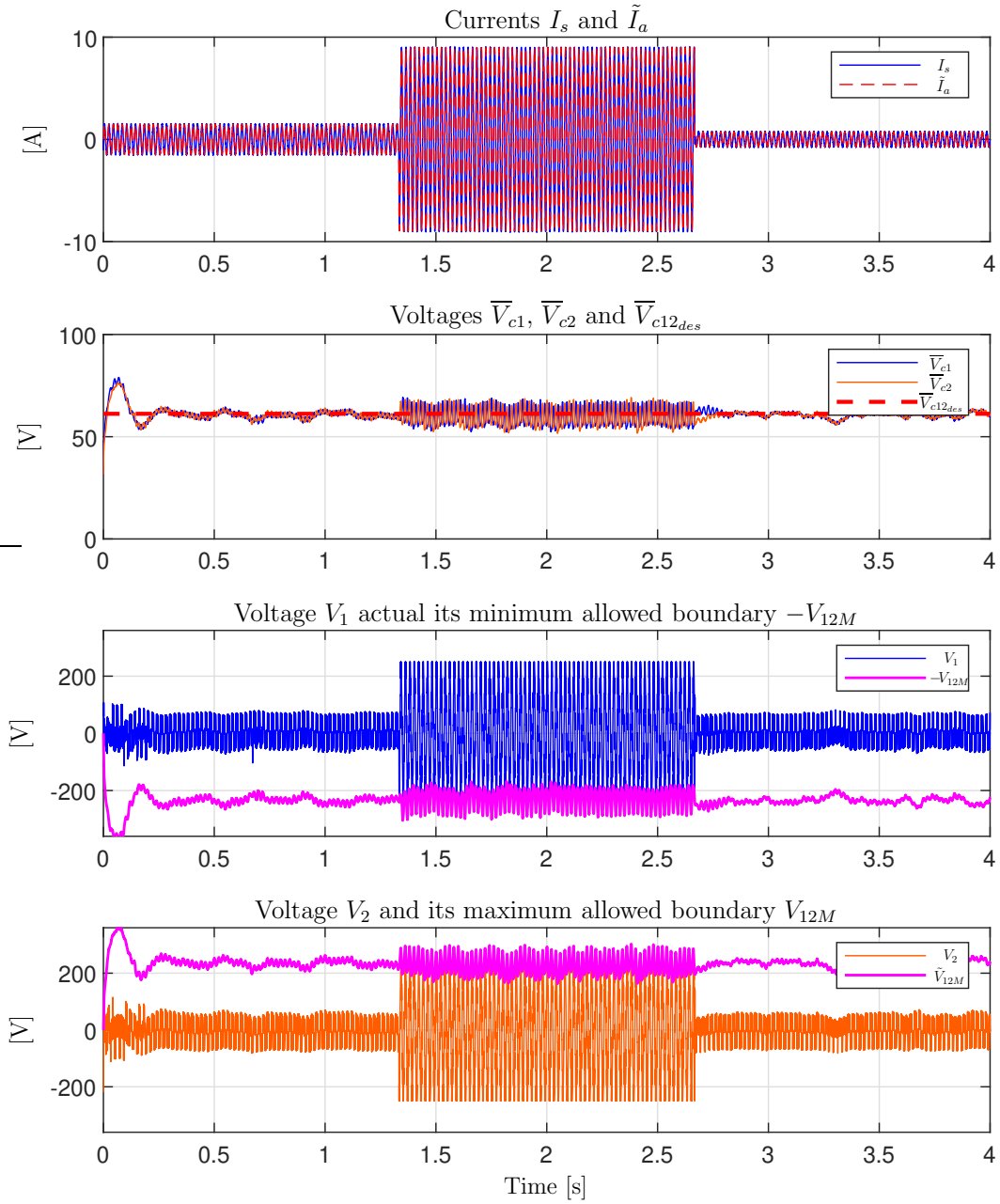


Figure 11: Results of the second simulation.

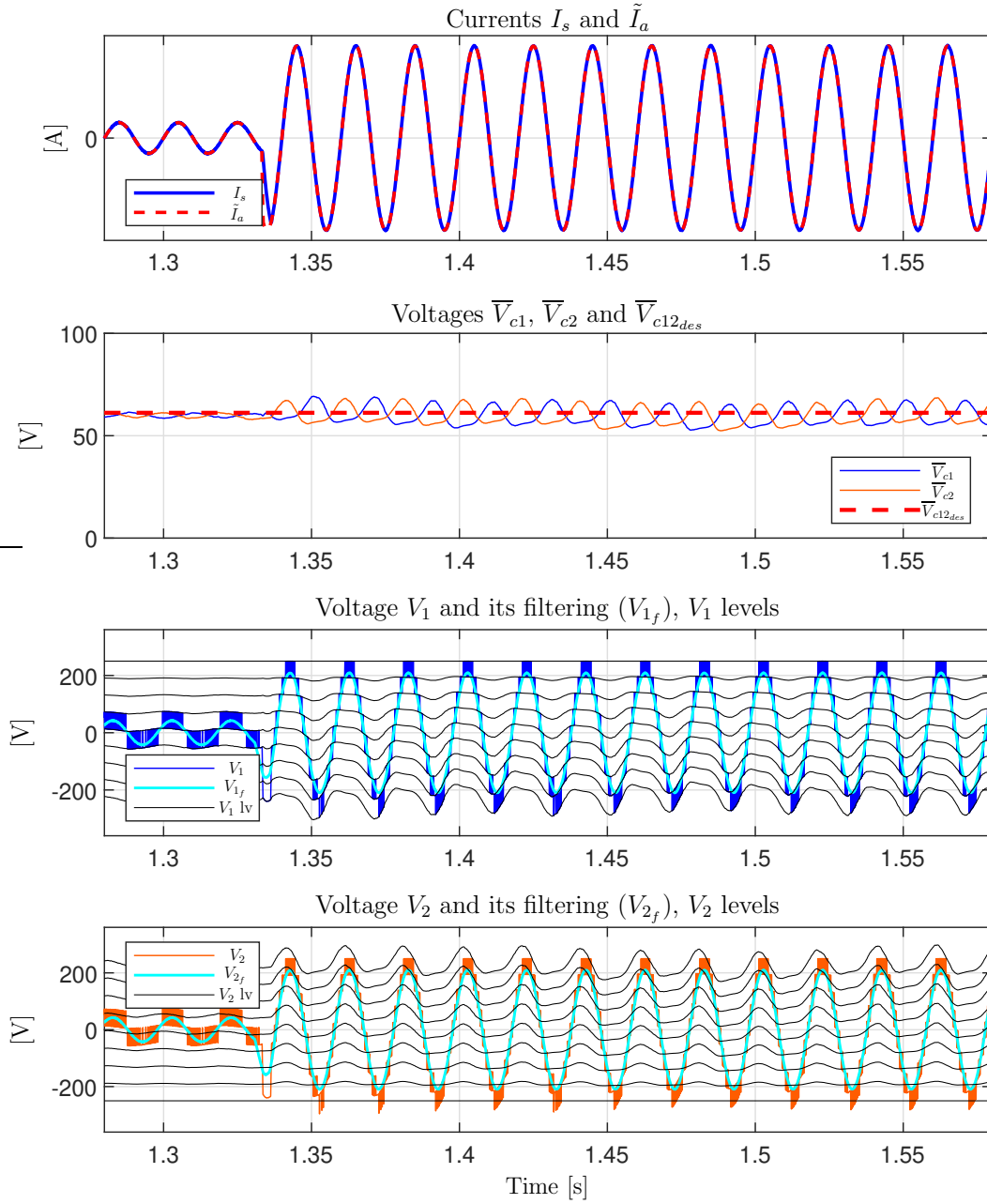


Figure 12: Results of the second simulation: zoom-in.

when the amplitude I_{aM} changes, as shown in the third and fourth subplots of Fig. 9. This proves the effectiveness of the approach described in Sec. 3.2.3 for the computation of the optimal voltage reference $\bar{V}_{c12_{des}}$ for voltages \bar{V}_{c1} and \bar{V}_{c2} . The capacitor voltages $V_{c_{i+(j-1)\times n}}$ for $i \in \{1, \dots, n\}$, in the lower and upper converter arms $j \in \{1, 2\}$, are kept balanced and equal to the corresponding mean values \bar{V}_{c1} and \bar{V}_{c2} by the algorithm in Fig. 6. The good tracking of the optimal reference $\bar{V}_{c12_{des}}$ by voltages \bar{V}_{c1} and \bar{V}_{c2} can be observed from the second subplot of Fig. 9, and shows: 1) The effectiveness of the algorithm proposed in Fig. 7 for the generation of the desired current \tilde{I}_d ; 2) the effectiveness of the optimal control problem in (40), which could be solved exactly thanks to the prediction described by the code in Fig. 8. Furthermore, Fig. 9 also shows the very good superposition between the desired load current \tilde{I}_a and the load current I_s .

The optimal voltage reference $\bar{V}_{c12_{des}}$ is computed using (35)-(36) as described in Sec. 3.2.3, and represents the minimum value which is strictly needed for voltage V_s to track the desired value \tilde{V}_s in (14), and for the load current I_a to track the desired value \tilde{I}_a . Note that it is very convenient to make voltages \bar{V}_{c1} and \bar{V}_{c2} follow $\bar{V}_{c12_{des}}$; this is true because larger \bar{V}_{c1} and \bar{V}_{c2} would cause the discrete voltage levels generating voltages V_1 and V_2 to be more distant from each other. As an example, Fig. 10 shows a zoom-in of Fig. 9 for $t \in [1.28, 1.58]$ s. Note that the transient on voltages \bar{V}_{c1} and \bar{V}_{c2} in correspondence of $I_{aM} = 1.5 \rightarrow 9$ A is very short. Furthermore, one can observe that the available voltage levels (black characteristics in the figure) generating voltages V_1 and V_2 are much closer to each other whenever I_{aM} is lower. This brings two important advantages: 1) a lower harmonic content in the resulting load current I_s ; 2) a better tracking of current I_s itself, leading to a cleaner sinusoid, as proved in the comparison with the second simulation.

Second Simulation: The results of the simulation using the constant reference $\bar{V}_{c12_{des}}$ are shown in Fig. 11 and Fig. 12. In this case, \bar{V}_{c1} and \bar{V}_{c2} have to track the constant reference $\bar{V}_{c12_{des}}$ representing the minimum value which is strictly needed to always track the desired \tilde{I}_a , that is the value of the optimal reference $\bar{V}_{c12_{des}}$ in the first simulation in the most demanding situation represented by the case $I_{aM} = 9$ A. Since $\bar{V}_{c12_{des}}$ is constant, from the zoomed-in results of Fig. 12, one can observe that the level-to-level distance when generating voltages V_1 and V_2 does not change throughout the simulation even when there would be room to reduce it, that is when I_{aM} decreases. This causes two main disadvantages: 1) a higher harmonic con-

Table 3: Metrics evaluating the resulting load current I_s in the first and second simulation.

t [s]	$\in [0.38, 0.4]$	$\in [2.14, 2.16]$	$\in [3.08, 3.1]$	
RMS(e_{I_a}) [mA]	25.0	28.19	24.43	Constant $\bar{V}_{c12_{des}}$
max($ e_{I_a} $) [mA]	56.4	81.4	54.8	
avg(fft(I_s)) [A]	1.82 (Ideal: 1.5)	9.33 (Ideal: 9)	1.04 (Ideal: 0.75)	
RMS(e_{I_a}) [mA]	14.97 (-40.12 %)	28.15 (-0.14 %)	13.44 (-44.99 %)	Optimized $\bar{V}_{c12_{des}}$
max($ e_{I_a} $) [mA]	39.06 (-30.74 %)	81.34 (-0.07 %)	30.95 (-43.52 %)	
avg(fft(I_s)) [A]	1.68 (Ideal: 1.5)	9.34 (Ideal: 9)	0.92 (Ideal: 0.75)	

tent in the resulting load current I_s ; 2) a worse tracking of the load current I_s itself. This can be verified by the results reported in Table 3, which contains the following three metrics for comparison: the root mean square value of the tracking error e_{I_a} on the load current I_s : $\text{RMS}(e_{I_a})$, the maximum absolute value of the tracking error e_{I_a} on the load current I_s : $\max(|e_{I_a}|)$, and the average value of the amplitude spectrum resulting after applying the Fast-Fourier Transform (FFT) on the load current I_s : $\text{avg}(\text{fft}(I_s))$. The FFT on the load current I_s has been computed using the “fft” Matlab function. These three metrics have been computed on the load current I_s for three different time intervals, corresponding to one period of the load current taken when $I_{aM} = 1.5$ A, $I_{aM} = 9$ A and $I_{aM} = 0.75$ A, respectively. Let us first consider the time interval $t \in [2.14, 2.16]$ s, corresponding to one period of the load current when $I_{aM} = 9$ A. In this case, Table 3 shows that $\text{RMS}(e_{I_a})$ is approximately the same both in the first simulation, in which the optimal reference $\bar{V}_{c12_{des}}$ is used for voltages \bar{V}_{c1} and \bar{V}_{c2} , and in the second simulation. This happens because the constant reference $\bar{V}_{c12_{des}}$ in the second simulation has indeed been set to the exact minimum value which is strictly needed to track a load current having an amplitude $I_{aM} = 9$ A. A similar observation applies to the metrics $\max(|e_{I_a}|)$ and $\text{avg}(\text{fft}(I_s))$. Let us now consider the time intervals $t \in [0.38, 0.4]$ s and $t \in [3.08, 3.1]$ s, corresponding to one period of the load current when $I_{aM} = 1.5$ A and $I_{aM} = 0.75$ A, respectively. In this case, one can observe that $\text{RMS}(e_{I_a})$ and $\max(|e_{I_a}|)$ are significantly larger in the second simulation (“Constant $\bar{V}_{c12_{des}}$ ” case) than

in the first simulation (“Optimized $\bar{V}_{c12_{des}}$ ” case), highlighting a tracking of the desired load current profile \tilde{I}_a which is much worse. This is due to the fact that voltages V_1 and V_2 are generated using larger discrete voltage levels, as shown in Fig. 12. This also implies a higher harmonic content in the generated load current I_s , as quantified by the quantity $\text{avg}(\text{fft}(I_s))$ in the second simulation with a constant $\bar{V}_{c12_{des}}$, which is more distant from the theoretical value that it should exhibit in the case of a pure sinusoid (1.5 A and 0.75 A, respectively) with respect to the first simulation. This proves the effectiveness of the approach for computing the optimal average capacitor voltages reference $\bar{V}_{c12_{des}}$ and of the model-based adaptive control proposed in this paper.

5. Conclusion

In this paper, we addressed the modeling, the harmonic analysis and the model-based adaptive control of MMCs. As far as the modeling part is concerned, we proposed a new compact block scheme to model MMCs, which is directly implementable in the Matlab/Simulink environment using simple blocks which are available in standard Simulink libraries. The proposed model has then been verified against the PLECS simulator. We then introduced two congruent state-space transformations in order to decouple the MMC dynamics, thus enabling the proposed harmonic analysis of modular multilevel converters. The performed harmonic analysis has given a deep and exact understanding of the MMC dynamics. Thanks to this, we could determine the optimal tracking reference for the circulating current in order to make the average capacitor voltages follow the desired reference, and we could compute exactly the optimal voltage reference for the average capacitor voltages in the upper and lower arms of the converter. Such optimal voltage reference represents the minimum value which is strictly necessary to properly track the desired load current while, at the same time, minimizing the harmonic content in the generated load current itself. The simulation results show how the new proposed model-based adaptive control allows to effectively achieve all the goals of the Control Problem at the same time: a) balancing of the capacitor voltages; b) tracking of the optimal voltage reference for the average capacitor voltages in order to minimize the harmonic content in the load current; c) tracking of the desired load current profile. The simulation results also show the effectiveness of one of the new important concepts that we have introduced in this paper, that is to adaptively

vary the average capacitor voltages in the upper and lower arms of the MMC thus making the proposed model-based control adaptive to the operating conditions. The circulating current is exploited in order to make the average capacitor voltages follow the optimal voltage reference which is adapted in real-time as a function of the desired load current. This represents a crucial advantage with respect to the classical approach of maintaining the average capacitor voltages at a constant value, because it enables the reduction of the harmonic content in the generated load current by minimizing the level-to-level distance in the commutating voltage signals, thus enhancing all the intrinsic main advantages of multilevel converters.

Funding

This research did not receive any specific grant from funding agencies in the public, commercial, or not-for-profit sectors.

Declaration of Generative AI and AI-assisted technologies in the writing process

During the preparation of this work the authors did not use any Generative AI and AI-assisted technologies in the writing process.

Appendix A: Sinusoidal behavior of function $P_1(t)$

Function $P_1(t)$ in (19) is composed of the three terms $2V_{dc}I_d$, V_dI_d and $f(t)\tilde{I}_a$. The first term $2V_{dc}I_d$ is known, see (22). The second term V_dI_d can be expressed as follows, see App. B:

$$V_d I_d = V_{d0} I_{d0} + \frac{V_{dM} I_{dM}}{2} \cos(\alpha_{LR}) + F_{V_d I_d}(\omega t), \quad (\text{A.1})$$

where $F_{V_d I_d}(\omega t)$ is the sum of two sinusoidal terms at frequency ω and 2ω , see (B.1). Function $f(t) = L_T \dot{\tilde{I}}_a + R_T \tilde{I}_a + 2V_a$ in (14) and (19) can be written as $f(t) = f_M \sin(\omega t + \alpha_f)$, see App. D, where:

$$f_M = \sqrt{S_f^2 + C_f^2}, \quad \alpha_f = \arctan\left(\frac{S_f}{C_f}\right), \quad (\text{A.2})$$

$S_f = L_T I_{aM} \omega + 2V_{aM} \sin(\alpha_{V_a})$ and $C_f = R_T I_{aM} + 2V_{aM} \cos(\alpha_{V_a})$. Using (E.1), the third term $f(t)\tilde{I}_a$ of function $P_1(t)$ can be expressed as follows:

$$f(t)\tilde{I}_a = f_M \sin(\omega t + \alpha_f) I_{aM} \sin(\omega t) = \frac{f_M I_{aM}}{2} \cos(\alpha_f) - \frac{f_M I_{aM}}{2} \cos(2\omega t + \alpha_f). \quad (\text{A.3})$$

From (14), (22), (A.1) and (A.3), it follows that function $P_1(t)$ can be rewritten as in (23).

Appendix B: Sinusoidal behavior of function $V_d I_d$

Using (21), (22) and (E.1), function $V_d I_d$ can be expressed as follows:

$$\begin{aligned} V_d I_d &= [V_{d0} + V_{dM} \sin(\omega t + \alpha_{V_d})] \cdot [I_{d0} + I_{dM} \sin(\omega t + \alpha_{V_d} - \alpha_{LR})] \\ &= V_{d0} I_{d0} + V_{dM} I_{dM} \sin(\omega t + \alpha_{V_d}) \cdot \sin(\omega t + \alpha_{V_d} - \alpha_{LR}) + F_1(\omega t) \\ &= V_{d0} I_{d0} + \frac{V_{dM} I_{dM}}{2} \cos(\alpha_{LR}) - \frac{V_{dM} I_{dM}}{2} \cos(2\omega t + 2\alpha_{V_d} - \alpha_{LR}) + F_1(\omega t) \\ &= V_{d0} I_{d0} + \frac{V_{dM} I_{dM}}{2} \cos(\alpha_{LR}) + F_{V_d I_d}(\omega t), \end{aligned}$$

where $F_1(\omega t) = I_{d0} V_{dM} \sin(\omega t + \alpha_{V_d}) + V_{d0} I_{dM} \sin(\omega t + \alpha_{V_d} - \alpha_{LR})$ and:

$$\begin{aligned} F_{V_d I_d}(\omega t) &= F_1(\omega t) - \frac{V_{dM} I_{dM}}{2} \cos(2\omega t + 2\alpha_{V_d} - \alpha_{LR}) \\ &= I_{d0} V_{dM} \sin(\omega t + \alpha_{V_d}) + V_{d0} I_{dM} \sin(\omega t + \alpha_{V_d} - \alpha_{LR}) \\ &\quad - \frac{V_{dM} I_{dM}}{2} \cos(2\omega t + 2\alpha_{V_d} - \alpha_{LR}). \end{aligned} \quad (\text{B.1})$$

Appendix C: Sinusoidal behavior of function $P_2(t)$

Function $P_2(t)$ in (19) is composed of the three terms $2V_{dc} \tilde{I}_a$, $V_d \tilde{I}_a$ and $f(t)I_d$. The first term $2V_{dc} \tilde{I}_a$ is known, see (20). Using (E.1), the second term $V_d \tilde{I}_a$ can be expressed as follows:

$$V_d \tilde{I}_a = [V_{d0} + V_{dM} \sin(\omega t + \alpha_{V_d})] I_{aM} \sin(\omega t) = \frac{V_{dM} I_{aM}}{2} \cos(\alpha_{V_d}) + F_2(\omega t), \quad (\text{C.1})$$

where $F_2(\omega t) = V_{d0} I_{aM} \sin(\omega t) - \frac{V_{dM} I_{aM}}{2} \cos(2\omega t + \alpha_{V_d})$. Using (E.1), the third term $f(t)I_d$ of function $P_2(t)$ can be expressed as follows:

$$\begin{aligned} f(t)I_d &= f_M \sin(\omega t + \alpha_f) [I_{d0} + I_{dM} \sin(\omega t + \alpha_{V_d} - \alpha_{LR})] \\ &= \frac{f_M I_{dM}}{2} \cos(\alpha_f - \alpha_{V_d} + \alpha_{LR}) + F_3(\omega t), \end{aligned} \quad (\text{C.2})$$

where $F_3(\omega t) = I_{d0} f_M \sin(\omega t + \alpha_f) - \frac{f_M I_{dM}}{2} \cos(2\omega t + \alpha_f + \alpha_{V_d} - \alpha_{LR})$. From (14), (20), (21), (C.1) and (C.2), it follows that function $P_2(t)$ can be expressed as in (27).

Appendix D: Sinusoidal behavior of function $f(t)$

Function $f(t)$ is the sum of three sinusoidal terms characterized by the same frequency ω , and can therefore be expressed as follows:

$$\begin{aligned}
f(t) &= L_T \dot{\tilde{I}}_a + R_T \tilde{I}_a + 2V_a = L_T I_{aM} \omega \cos(\omega t) + R_T I_{aM} \sin(\omega t) + 2V_{aM} \sin(\omega t + \alpha_{V_a}) \\
&= L_T I_{aM} \omega \cos(\omega t) + R_T I_{aM} \sin(\omega t) + 2V_{aM} \sin(\omega t) \cos(\alpha_{V_a}) + 2V_{aM} \cos(\omega t) \sin(\alpha_{V_a}) \\
&= [R_T I_{aM} + 2V_{aM} \cos(\alpha_{V_a})] \sin(\omega t) + [L_T I_{aM} \omega + 2V_{aM} \sin(\alpha_{V_a})] \cos(\omega t) \\
&= f_M \sin(\omega t + \alpha_f),
\end{aligned}$$

where $f_M = \sqrt{S_f^2 + C_f^2}$, $\alpha_f = \arctan\left(\frac{S_f}{C_f}\right)$, $S_f = L_T I_{aM} \omega + 2V_{aM} \sin(\alpha_{V_a})$ and $C_f = R_T I_{aM} + 2V_{aM} \cos(\alpha_{V_a})$.

Appendix E: Product of two sinusoidal functions

The product $F_1(t)F_2(t)$ of two sinusoidal signals $F_1(t) = a_1 \sin(\omega t + \alpha_1)$ and $F_2(t) = a_2 \sin(\omega t + \alpha_2)$ can always be written as follows:

$$\begin{aligned}
F_1(t)F_2(t) &= a_1 a_2 \sin(\omega t + \alpha_1) \sin(\omega t + \alpha_2) \\
&= \frac{a_1 a_2}{2} \cos(\alpha_1 - \alpha_2) - \frac{a_1 a_2}{2} \cos(2\omega t + \alpha_1 + \alpha_2).
\end{aligned} \tag{E.1}$$

Appendix F: The constant term P_{20}

Using (22), the constant term P_{20} can also be expressed as follows:

$$\begin{aligned}
P_{20} &= -\frac{V_{dM} I_{aM}}{2} \cos(\alpha_{V_d}) - \frac{f_M I_{dM}}{2} \cos(\alpha_{V_d} - \alpha_f - \alpha_{LR}) \\
&= -\frac{V_{dM} I_{aM}}{2} \cos(\alpha_{V_d}) - \frac{V_{dM} f_M}{2\sqrt{R^2 + L^2 \omega^2}} \cos(\alpha_{V_d} + \beta) \\
&= -\frac{V_{dM} I_{aM}}{2} \cos(\alpha_{V_d}) + \frac{V_{dM} f_M}{2\sqrt{R^2 + L^2 \omega^2}} [\cos(\alpha_{V_d}) \cos(\beta) - \sin(\alpha_{V_d}) \sin(\beta)] \\
&= -\frac{V_{dM}}{2} \underbrace{\left(I_{aM} + \frac{f_M \cos(\beta)}{\sqrt{R^2 + L^2 \omega^2}} \right)}_a \cos(\alpha_{V_d}) + \frac{V_{dM}}{2} \underbrace{\frac{f_M \sin(\beta)}{\sqrt{R^2 + L^2 \omega^2}}}_b \sin(\alpha_{V_d}) \\
&= -\frac{V_{dM} \sqrt{a^2 + b^2}}{2} [\cos(\gamma) \cos(\alpha_{V_d}) - \sin(\gamma) \sin(\alpha_{V_d})] = -\frac{V_{dM} \sqrt{a^2 + b^2}}{2} \cos(\alpha_{V_d} + \gamma),
\end{aligned}$$

where $\beta = -\alpha_f - \alpha_{LR}$, $a = \cos(\gamma)$, $b = \sin(\gamma)$ and $\gamma = \arctan 2(b, a)$. The values of parameters f_M and α_f have been defined in (A.2), and the value of parameter α_{LR} has been defined in (22).

References

- [1] M. Romero-Rodríguez, R. Delpoux, L. Piétrac, J. Dai, A. Benchaib, E. Niel, “An implementation method for the supervisory control of time-driven systems applied to high-voltage direct current transmission grids”, *Control Engineering Practice*, vol. 82, pp. 97-107, Jan. 2019, DOI: 10.1016/j.conengprac.2018.10.002.
- [2] M. Emin Meral, D. Çelik, “Proportional complex integral based control of distributed energy converters connected to unbalanced grid system”, *Control Engineering Practice*, vol. 103, Oct. 2020, DOI: 10.1016/j.conengprac.2020.104574.
- [3] R. Zanasi, D. Tebaldi, “Modeling of complex planetary gear sets using power-oriented graphs”, *IEEE Trans. Veh. Technol.*, vol. 69, no. 12, pp. 14470-14483, Dec. 2020, DOI: 10.1109/TVT.2020.3040899.
- [4] D. Tebaldi, R. Zanasi, “Systematic modeling of complex time-variant gear systems using a Power-Oriented approach”, *Control Engineering Practice*, vol. 132, Mar. 2023, DOI: 10.1016/j.conengprac.2022.105420.
- [5] W. He, Y. Shang, M. Masoud Namazi, R. Ortega, “Adaptive sensorless control for buck converter with constant power load”, *Control Engineering Practice*, vol. 126, Sep. 2022, DOI: 10.1016/j.conengprac.2022.105237.
- [6] Q. Guo, I. Bahri, D. Diallo, E. Berthelot, “Model predictive control and linear control of DC-DC boost converter in low voltage DC micro-grid: An experimental comparative study”, vol. 131, Feb. 2023, DOI: 10.1016/j.conengprac.2022.105387.
- [7] J. Saeed, L. Wang, N. Fernando, “Model predictive control of phase shift full-bridge DC-DC converter using laguerre functions”, *IEEE Trans. Control Syst. Technol.*, vol. 30, no. 2, pp. 819-826, Mar. 2022, DOI: 10.1109/TCST.2021.3069148.
- [8] R. Cisneros, M. Pirro, G. Bergna, R. Ortega, G. Ippoliti, M. Molinas, “Global tracking passivity-based PI control of bilinear systems: Application to the interleaved boost and modular multilevel converters”, *Control Engineering Practice*, vol. 43, pp. 109-119, Oct. 2015, DOI: 10.1016/j.conengprac.2015.07.002.

- [9] M. Kamarzarrin, M. Hossein Refan, P. Amiri, “Open-circuit faults diagnosis and Fault-Tolerant Control scheme based on Sliding-Mode Observer for DFIG back-to-back converters: wind turbine applications”, *Control Engineering Practice*, vol. 126, Sep. 2022, DOI: 10.1016/j.conengprac.2022.105235.
- [10] R. Zanasi, D. Tebaldi, “Modeling control and robustness assessment of multilevel flying-capacitor converters”, *Energies*, 2021, 14(7), 1903, DOI: 10.3390/en14071903.
- [11] A. Bouarfa, M. Bodson, M. Fadel, “An optimization formulation of converter control and its general solution for the four-leg two-level inverter”, *IEEE Trans. Control Syst. Technol.*, vol. 26, no. 5, pp. 1901-1908, Sep. 2018, DOI: 10.1109/TCST.2017.2738608.
- [12] J.-N. Chiasson, L.-M. Tolbert, K.-J. McKenzie, Z. Du, “Control of a multilevel converter using resultant theory”, *IEEE Trans. Control Syst. Technol.*, vol. 11, no. 3, pp. 345-354, May. 2003, DOI: 10.1109/TCST.2003.810382.
- [13] J.-N. Chiasson, L.-M. Tolbert, K.-J. McKenzie, Z. Du, “Elimination of harmonics in a multilevel converter using the theory of symmetric polynomials and resultants”, *IEEE Trans. Control Syst. Technol.*, vol. 13, no. 2, pp. 216-223, Mar. 2005, DOI: 10.1109/TCST.2004.839556.
- [14] S. Laamiri, M. Ghanes, G. Santomenna, “Observer based direct control strategy for a multi-level three phase flying-capacitor inverter”, *Control Engineering Practice*, vol. 86, pp. 155-165, May 2019, DOI: 10.1016/j.conengprac.2019.03.011.
- [15] L. Hetel, M. Defoort, M. Djemai, “Binary control design for a class of bilinear systems: application to a multilevel power converter”, *IEEE Trans. Control Syst. Technol.*, vol. 24, no. 2, pp. 719-726, Mar. 2016, DOI: 10.1109/TCST.2015.2460696.
- [16] M. Diaz, R. Cardenas, E. Ibaceta, A. Mora, M. Urrutia, M. Espinoza, F. Rojas, P. Wheeler, “An overview of modelling techniques and control strategies for modular multilevel matrix converters”, *Energies*, 2020, 13(18), 4678, DOI: 10.3390/en13184678.

- [17] M. Liu, Z. Li, X. Yang, “A universal mathematical model of modular multilevel converter with half-bridge”, *Energies*, 2020, 13(17), 4464, DOI: 10.3390/en13174464.
- [18] P. Delarue, F. Gruson, X. Guillaud, “Energetic macroscopic representation and inversion based control of a modular multilevel converter”, *15th European Conference on Power Electronics and Applications (EPE)*, Lille, France, Sep. 2-6, 2013, DOI: 10.1109/EPE.2013.6631859.
- [19] P.-B. Steckler, J.-Y. Gauthier, X. Lin-Shi, F. Wallart, “Differential flatness-based, full-order nonlinear control of a modular multilevel converter (MMC)”, *IEEE Trans. Control Syst. Technol.*, vol. 30, no. 2, pp. 547-557, Mar. 2022, DOI: 10.1109/TCST.2021.3067887.
- [20] S. Du, J. Liu, T. Liu, “Modulation and closed-loop-based DC capacitor voltage control for MMC with fundamental switching frequency”, *IEEE Trans. Power Electron.*, vol. 30, no. 1, pp. 327-338, Jan. 2015, DOI: 10.1109/TPEL.2014.2301836.
- [21] A. Abdayem, J. Sawma, F. Khatounian, E. Monmasson, “Control of a single phase modular multilevel converter based on a new modulation technique”, *22nd IEEE International Conference on Industrial Technology (ICIT)*, Valencia, Spain, Mar. 10-12, 2021, DOI: 10.1109/ICIT46573.2021.9453516.
- [22] L. Ben-Brahim, A. Gastli, M. Trabelsi, K.-A. Ghazi, M. Houchati, H. Abu-Rub, “Modular multilevel converter circulating current reduction using model predictive control”, *IEEE Trans. Ind. Electron.*, vol. 63, no. 6, pp. 3857-3866, Jun. 2016, DOI: 10.1109/TIE.2016.2519320.
- [23] B. S. Riar, T. Geyer, U. K. Madawala, “Model predictive direct current control of modular multilevel converters: modeling, analysis, and experimental evaluation”, *IEEE Trans. Power Electron.*, vol. 30, no. 1, pp. 431-439, Jan. 2015, DOI: 10.1109/TPEL.2014.2301438.
- [24] L. Harnefors, A. Antonopoulos, S. Norrga, L. Ängquist, H.-P. Nee, “Dynamic analysis of modular multilevel converters”, *IEEE Trans. Ind. Electron.*, vol. 60, no. 7, pp. 2526-2537, Jul. 2013, DOI: 10.1109/TIE.2012.2194974.

- [25] R. Zanasi, “The power-oriented graphs technique: system modeling and basic properties”, *Proceedings of IEEE Vehicle Power and Propulsion Conference (VPPC)*, Lille, France, Sep. 1-3, 2010, DOI: 10.1109/VPPC.2010.5729018.
- [26] M.-S. Jha, G. Dauphin-Tanguy, B. Ould-Bouamama, “Robust fault detection with interval valued uncertainties in bond graph framework”, *Control Engineering Practice*, vol. 71, pp. 61-78, Feb. 2018, DOI: 10.1016/j.conengprac.2017.10.009.
- [27] A. Badoud, M. Khemliche, S. Bacha, B. Raison, “Modeling and performance analysis of multilevel inverter for single-phase grid connected photovoltaic modules”, *International Renewable and Sustainable Energy Conference (IRSEC)*, Ouarzazate, Morocco, Mar. 7-9, 2013, DOI: 10.1109/IRSEC.2013.6529727.
- [28] I. García-Herreros, X. Kestelyn, J. Gomand, R. Coleman, P.-J. Barre, “Model-based decoupling control method for dual-drive gantry stages: a case study with experimental validations”, *Control Engineering Practice*, vol. 21, no. 3, pp. 298-307, Mar. 2013, DOI: 10.1016/j.conengprac.2012.10.010.
- [29] D. Tebaldi, “Efficiency map-based PMSM parameters estimation using power-oriented modeling”, *IEEE Access*, vol. 10, pp. 45954-45961, Apr. 2022, DOI: 10.1109/ACCESS.2022.3169149.
- [30] D. Tebaldi, R. Zanasi, “Modeling and simulation of a multiphase diode bridge rectifier”, *IEEE European Control Conference (ECC)*, St. Petersburg, Russia, May 12-15, 2020, DOI: 10.23919/ECC51009.2020.9143693.
- [31] PLECS Documentation: <https://www.plexim.com/products/plecs>.